Seasonal spatial patterns of projected anthropogenic warming in complex terrain: A modeling study of the western US

David E. Rupp[1], Sihan Li[1], Philip W. Mote[1], Karen M. Shell[2], Neil Massey[3], Sarah N. Sparrow[4], David C. H. Wallom[4], and Myles R. Allen[3,5]

[1]Oregon Climate Change Research Institute, College of Earth, Ocean, and Atmospheric Science, Oregon State University, Corvallis, Oregon, US

[2]College of Earth, Ocean, and Atmospheric Science, Oregon State University, Corvallis, Oregon, US

[3]Environmental Change Institute, School of Geography and the Environment, University of Oxford, Oxford, UK

[4]Oxford e-Research Centre, University of Oxford, Oxford, UK

[5]Atmospheric, Oceanic and Planetary Physics, Department of Physics, University of Oxford, Oxford, UK

Corresponding author: D. Rupp, Oregon Climate Change Research Institute, College of Earth, Ocean, and Atmospheric Science, Oregon State University, Corvallis, Oregon 97331, USA. (david.rupp@oregonstate.edu)

Prepared for submission to *Climate Dynamics*, May, 2016

Abstract

Changes in near surface air temperature (ΔT) in response to anthropogenic greenhouse gas forcing are expected to show spatial heterogeneity because energy and moisture fluxes are modulated by features of the landscape that are also heterogeneous at these spatial scales. Detecting statistically meaningful heterogeneity requires a combination of high spatial resolution and a large number of simulations. To investigate spatial variability of projected ΔT, we generated regional, high-resolution (25-km horizontal), large ensemble (100 members per year), climate simulations of western United States (US) for the periods 1985 – 2014 and 2030 – 2059, the latter with atmospheric constituent concentrations from the Representative Concentration Pathway 4.5. Using the large ensemble, 95% confidence interval sizes for grid-cell-scale temperature responses were on the order of 0.1 °C, compared to 1 °C from a single ensemble member only. In both winter and spring, the snow-albedo feedback statistically explains roughly half of the spatial variability in ΔT. Simulated decreases in albedo exceed 0.1 in places, with rates of change in T per 0.1 decrease in albedo ranging from 0.3 to 1.4 °C. In summer, ΔT pattern in the northwest US is correlated with the pattern of decreasing precipitation. In all seasons, changing lapse rates in the low-to-middle troposphere may account for up to 0.2 °C differences in warming across the western US. Near the coast, a major control of spatial variation is the differential warming between sea and land.

Keywords: Regional climate modeling; seasonal temperature projections; RCP 4.5; western US

41 **1 Introduction**

42 Changes in near surface air temperature in response to anthropogenic greenhouse gas
43 (GHG) forcing are expected to show meso- and local-scale heterogeneity because energy
44 and water fluxes are modulated by features of the landscape (topography, soil, and land
45 cover) that are also heterogeneous at these spatial scales (e.g., Giorgi et al. 1997;
46 Diffenbaugh et al. 2005; Salathé et al. 2008; Daly et al. 2010; Kotlarski et al. 2012). In
47 complex, mountainous terrain, such as the western United States (US), orography will
48 induce spatial variability in the snow-albedo feedback on temperature, cloud feedbacks
49 on temperature will be modified by the interaction of changing large-scale circulation and
50 the terrain, and spatially varying soil hydraulic properties and vegetation will affect the
51 magnitude of soil moisture feedbacks (Diffenbaugh et al. 2005). Changing large-scale
52 circulation may also alter the degree and frequency of cold air pooling in valleys (Daly et
53 al. 2010). A changing free air lapse rate in the lower to middle troposphere (Ramanathan
54 et al. 1979; Bradley et al. 2004) can leave a heterogeneous imprint on the land surface
55 with large topographic relief. Also, differential warming between sea and land, a robust
56 result of climate models (e.g., Sutton et al. 2007; Joshi et al. 2008), will produce a
57 warming gradient across some distance from the coast towards the interior.

58 Regional climate models (RCMs) with horizontal resolutions at least as fine as 50 km
59 have been widely used to quantify the net effect of various feedbacks and examine the
60 resulting spatial patterns of changes in temperature worldwide (e.g., Christensen and
61 Christensen 2007; van der Linden and Mitchell 2009; Boulanger et al. 2010; Mearns et al.
62 2013). The RCMs are nested within global climate models (GCMs) of much coarser

63 resolution that provide the lateral boundary conditions for the RCM. The information is
64 usually passed one-way only - from GCM to RCM; this procedure is called dynamical
65 downscaling.

66 The spread across models' regional projections of climate change for a given change in
67 anthropogenic forcing can be separated into two sources: model-sourced spread,
68 sometimes called uncertainty, and internal variability (Hawkins and Sutton 2009; 2011).
69 Model-sourced uncertainty reflects our incomplete understanding of the earth system,
70 computational constraints, and other practical limitations that result in simplified
71 representations of the earth system. Here we combine model structure, parameterizations
72 of small-scale processes that are not explicitly resolved, and model parameter values
73 together as contributors to model-sourced uncertainty. Internal variability arises from the
74 chaotic dynamics of the system of differential equations that are used to describe the
75 earth system, such that even a very small change in initial conditions (ICs) will lead to a
76 different trajectory of model states and fluxes (i.e., the butterfly effect; Lorenz 1963) and
77 even to different long-term means. Given sufficient realizations of an experiment with
78 varying ICs, however, the anthropogenically forced signal can be distinguished from the
79 noise of internal variability because the larger sample size can provide a more robust
80 estimate of the statistic being examined. What constitutes "sufficient" depends on the
81 variable, the magnitude of the change in the external forcing (and lead time if the
82 experiment is transient), the statistic, and the prescribed acceptable level of confidence
83 (Deser et al. 2012; 2014).

84 For those regional modeling studies that include the western US, nearly all published
85 projections of future (i.e., mid to late 21st century) climate from a unique RCM-GCM
86 coupling and radiative forcing scenario are limited to a single IC ensemble member
87 (Giorgi et al. 1994; Leung and Ghan 1999; Diffenbaugh et al. 2005; Duffy et al. 2006;
88 Liang et al. 2006; Plummer et al. 2006; Salathé et al. 2008; 2010; Hostetler et al. 2011;
89 Mearns et al. 2013; Šeparović et al. 2013; Wang and Kotamarthi 2015). The result is that
90 the particular spatial patterns of change presented in these studies may reflect the models'
91 internal variability to a high degree, largely masking the anthropogenic signal; the
92 question of what is a sufficient number of IC ensemble members to detect an
93 anthropogenic signal is rarely asked (O'Brien et al. 2010). Some studies examined
94 changes from several RCM-GCM pairings (Duffy et al. 2006; Hostetler et al. 2011;
95 Mearns et al. 2013), but this does not improve the understanding about how a particular
96 RCM-GCM responds to a change in forcing.

97 Much of the RCM development effort has been towards increasing the horizontal
98 resolution. For example, Wang and Kotamarthi (2015) presented climate projections for
99 the 21st century over North America using an RCM with a 12-km resolution. RCMs have
100 been applied at yet much higher resolutions, but over much smaller regions. Examples
101 include resolutions of 2 km over the Colorado Headwaters region (Rasmussen et al.
102 2011), 3 km over the central Sierra Nevada, California (Pavelsky et al. 2013), 1.3 km
103 over the Colorado Front Range (Mahoney et al. 2013), and 0.5 km over Weymouth and
104 Portland Harbor, United Kingdom (Wang et al. 2013).

105 In contrast, less progress has been made towards increasing IC ensemble size. Two
106 examples of progress are the 3-member and 5-member IC ensembles of Leung et al.
107 (2004) and Diffenbaugh et al. (2011), respectively. Mote et al. (2015), using the same
108 modeling framework as presented here, made the most pointed effort at increasing signal-
109 to-noise ratio, describing an experiment to generate IC ensembles of hundreds to
110 thousands of members using a volunteer computing network.

111 In this paper, we report results from simulations with an RCM-GCM pair for a recent
112 historical period (Dec. 1985 – Nov. 2014) and a future period that spans the mid-21st
113 century (Dec. 2030 – Nov. 2059). Each year's model output consists of 100 IC ensemble
114 members, for a total 2,900 years of simulations for each the historical and future periods.
115 This large ensemble size allows for a very large reduction in the standard error due to
116 internal variability (though errors from model-sourced uncertainty and the unknown
117 future forcing are still present). This paper begins the first detailed study of climate
118 projections that combines both high horizontal resolution (25 km) and a very large IC
119 ensemble.

120 We describe patterns of anthropogenically forced spatial patterns of change in seasonal
121 mean temperature (changes in various quantiles of temperature and precipitation will be
122 presented in subsequent papers). The range of temperature change across a region may
123 be of the same order of magnitude as the regionally-averaged temperature change itself,
124 and thus have relevance to human society and ecosystems. We identify some dominant
125 factors that determine meso-scale spatial patterns: changes in surface albedo,
126 tropospheric lapse rate, and precipitation rate, and the difference between sea and land

warming. Some of these factors have been previously documented in studies of the western US, namely the effect of changing albedo due to snowpack depletion (Leung et al. 2004; Diffenbaugh et al. 2005; Salathé et al. 2008; 2010). However, we go beyond a qualitative description of the factors and quantify the amount of spatial variance of temperature change that they explain.

2 Materials and Methods

This experiment relied on the Weather@home distributed volunteer computing project to generate large IC ensembles of regional climate simulations (Massey et al. 2014; Mote et al. 2015). Weather@home uses the U.K. Met Office Hadley Centre's regional climate model HadRM3P nested within the atmospheric global model HadAM3P. HadRM3P is integrated with a 5-minute timestep over a horizontal resolution of 0.22° latitude (~25 km), while HadAM3P is integrated with a 15-minute timestep and has a horizontal resolution of 1.875° longitude by 1.25° latitude (~139 km latitudinally). HadRM3P and HadAM3P are run concurrently (HadAM3P/RM3P), with HadAM3P providing the lateral boundary conditions to HadRM3P once each simulated day (the coupling is one-way only). HadAM3P/RM3P built for this experiment uses the MOSES1 land surface model (Cox et al. 1999). Massey et al. (2014) provided a detailed description of the Weather@home system, and particulars about the western US domain configuration were given in Mote et al. (2015) and Li et al. (2015). Several studies examined the ability of HadRM3P (Zhang et al. 2009; Dulière et al. 2011; 2013) and the HadAM3P/RM3P configuration used in Weather@home (Mote et al. 2015; Li et al. 2015) to reproduce various properties of the recent past climate of the northwestern and western US. Mote et

149 al. (2015) summarized limitations of Weather@home, such as that sea surface
150 temperatures are specified instead of generated by coupling to an ocean circulation
151 model. Li et al. (2015) quantified differences between the historical simulations with
152 HadAM3P/RM3P and observation-based data (North American Regional Reanalysis;
153 Mesinger et al. 2006), showing high spatial correlation *r* in mean seasonal temperature
154 across the western US, with *r* ranging from 0.96 in summer to 0.99 in fall. They also
155 showed that regionally averaged seasonal temperature biases were less than +/- 1 °C from
156 fall through spring, and the bias in summer was 1.7 °C.

157 For this study, a recent historical period (Dec. 1985 - Nov. 2014) and a future climate
158 scenario (Dec. 2030 – Nov. 2059) were simulated. Atmospheric forcings followed those
159 in the Coupled Model Intercomparison Project Phase 5 (CMIP5) *historical* and *RCP 4.5*
160 experiments (Taylor et al. 2011), respectively. The *RCP 4.5* scenario assumes mitigation
161 strategies are implemented such that radiative forcing is stabilized at 4.5 W m^{-2} above
162 pre-industrial levels by 2100 (Meinshausen et al. 2011). For this experiment, the increase
163 in total anthropogenic radiative forcing between the historical and future periods was 1.7
164 W m^{-2}. Though only *RCP 4.5* forcings were used for the current set of simulations, we
165 anticipate additional simulations using the more aggressive *RCP 8.5* scenario will be
166 done. One, however, can make a first-order approximation that the temperature response
167 is linear over a small range of forcing. Based on the same years used in the current
168 experiment, the increase in radiative forcing between the historical and future period
169 under *RCP 8.5* would be 2.5 W m^{-2}, which amounts to about a 47% greater increase in
170 temperature than under this *RCP 4.5* experiment.

Non-stationary forcings included in the model were greenhouse gas (GHG) concentrations, solar irradiance, volcanic aerosol optical depth, ozone concentrations, and sulphur dioxide emissions. The well-mixed GHGs considered were CO_2, CH_4, N_2O, and fluorinated gases expressed as HFC134a and CFC-12 equivalent concentrations.

Not coupling to an ocean model allows us to constrain one important source of variability in the simulations and increase comparability between simulations of the past and future. The consequence is that time-varying sea surface temperature (SST) and sea ice fraction were prescribed at each model ocean grid cell. For the historical period, the Operational Sea Surface Temperature and Sea Ice Analysis (OSTIA; Donlon et al. 2012) provided the SSTs and sea ice fractions. The OSTIA record begins in 1985, which is why we began the historical simulations that year.

SSTs for the future scenario were generated using a "delta" (Δ) method: smoothed changes in SSTs (ΔSSTs) from the historical to the future period were added to the OSTIA SSTs. The ΔSSTs were derived from the global model CESM1-CAM5 using ensemble member *r3i1p1* for the *historical* and *RCP 4.5* experiments in the CMIP5 archive. See Appendix A for details and see Fig. S1 in Supplementary Material for maps of average seasonal ΔSSTs.

Sea ice fractions for the future scenario were taken directly from monthly sea ice fraction from CESM1-CAM5 *r3i1p1 RCP 4.5*, modified to conform to the HadAM3P grid, land mask, and temporal resolution, using the method in Massey et al. (2014).

191 We chose CESM1-CAM5 to provide future sea ice fractions because it simulates
192 historical (1986–2005) mean Arctic sea ice extent with little bias compared to
193 observations (Meehl et al. 2013) and has less bias than most other CMIP5 GCMs, based
194 on Scheffield et al. (2014) and our own visual inspection (not shown). For consistency,
195 CESM1-CAM5 was also used for deriving the ΔSSTs. Moreover, Rupp et al. (2013)
196 found CESM1-CAM5 to rank best (least overall error) in an assessment of 41 CMIP5
197 GCMs based on a suite of performance metrics that, while focused on the climate of
198 Pacific Northwest, included seasonal temperature and precipitation patterns over the
199 northeast Pacific Ocean and western North America.

200 HadAM3P/RM3P was spun-up for the historical period and future scenario to bring land
201 surface states (e.g., soil moisture) to levels in loose quasi-equilibrium with the
202 atmospheric forcings. See Appendix B for a description of the spin-up procedure.

203 Simulations were one-year long, beginning December 1 and ending November 30. For
204 each year, a single base set of initial conditions was generated from one arbitrarily
205 selected simulation of the prior year. A large ensemble of atmospheric initial conditions
206 for each year was then generated by perturbing the three-dimensional potential
207 temperature field in the base set of initial conditions while all other states remained
208 unperturbed, as described in Massey et al. (2014). In total, 99 atmospheric initial
209 condition perturbations were applied to each December 1 base conditions to obtain
210 29(1+99) = 2,900 years of simulations for both the historical period and the future
211 scenario. A consequence of perturbing the initial conditions each year is that we did not
212 generate ensembles consisting of 29 years of continuous simulations. The advantage of

213 the Weather@home system, however, is that a very large number of simulations were
214 retrieved from volunteers in a relatively short amount of time (e.g. several weeks)
215 because we did not wait for one year-long simulation to complete before simulating the
216 following year.

217 For both the historical and future periods, we computed seasonal means of temperature
218 and other diagnostic variables (surface albedo, lapse rate, precipitation rate, surface
219 energy fluxes, soil moisture, etc.) by averaging the values over all 29 years and all 100
220 ensemble members for each RCM grid point. We then differenced the historical and
221 future scenario ensemble mean seasonal values to obtain the spatial pattern of climate
222 change (e.g., the temperature change, ΔT). By averaging over all years and all ensemble
223 members, our objective was to identify some consistent properties in the mean climate
224 response to changing forcing, with high signal-to-noise ratio. We acknowledge that
225 interesting and important properties of the climate response may be lost in the averaging.

226 For temperature, we also constructed three longitudinal transects; to assess the effect of
227 ensemble size, 95% confidence intervals on ΔT were estimated using bootstrapping,
228 assuming ensemble sizes of n = 1, 5, and 100 per year. During bootstrapping, each year
229 was sampled n times with replacement, and the entire transect of values for that year and
230 ensemble member were sampled together as group. The standard bootstrapping we used
231 does not explicitly account for the potential effect of year-to-year temporal
232 autocorrelation on the effective number of degrees of freedom, so our estimated
233 confidence intervals may be slightly too narrow. Note that because simulations were not
234 continuous (i.e., unperturbed) from one year to the next, we miss some of the temporal

autocorrelation in the atmospheric system (which has a decorrelation time scale of roughly a few weeks), though autocorrelation driven by the time-changing prescribed boundary conditions (e.g., SSTs) and forcings remains. It should be noted that these confidence intervals apply only to the internal variability of the model, which may not match the real world internal variability and that the confidence intervals do not include model-sourced uncertainty.

The lower-to-middle tropospheric lapse rate, $\Gamma = -dT/dz$, was approximated by taking the difference in T between the between the 850-hPa and 500-hPa geopotential height (z), because these were the only pressure levels on which both temperature and geopotential height were saved from the simulations. These heights correspond very roughly to 1.5 km and 5.5 km above mean sea level, respectively. Where the land surface was above 850 hPa, the lapse rate was not computed.

To aid in summarizing the data for analyses, the modeling domain was divided into 6 regions (see Fig. 1): Oregon and Washington west of, and including, the Cascade Range divide (Western OR/WA); Oregon and Washington east of the cascade divide (Eastern OR/WA); Idaho, Montana and Wyoming north of 42°N and west of 108°W (Northwest interior); California west of the Sierra Nevada and Cascade Range divides (Western CA); California east of the Sierra Nevada and Cascade Range divides (Eastern CA); Nevada, Utah, and Arizona north of 32.5°N, including the southwest corner of Wyoming (Southwest interior).

For comparison with the historical simulations, we used gridded observations of temperature from the 4-km resolution PRISM dataset (Daly et al. 2008). PRISM data were regridded to the coarser HadRM3P grid. PRISM provides daily minimum and maximum temperatures, which were averaged to approximate the mean temperature. Because the average of the daily minimum and maximum temperatures is not an exact measure of the daily mean temperature, which is the integral across the model time steps, it is an additional source of error.

3 Spatial Patterns of Seasonal Warming

Averaged over the western US (west of -109 °E), the simulated warming between the historical and future periods is 1.8 °C. The warming varies by a few tenths of a degree among seasons, with winter (December through February, DJF) and spring (March through May, MAM), warming least (1.7 °C), summer (June through July, JJA) warming the most (2.1 °C), and fall (September through November, SON) warming only slightly greater than winter and spring (1.8 °C).

The spatial pattern of warming also varies between seasons. In winter and spring, areas of largest ΔT are dispersed across the western US and in some places can be clearly associated with mountain ranges, such as the Cascades, Sierras, and the Wasatch and Uinta mountain ranges through central and northeast Utah (compare Fig. 1 with Figs. 2a and b). In contrast, the dominant features of warming in summer are a continental-scale gradient from Mexico to Canada and a gradient from coast to the interior to within 100 to 300 km of the coast, so that a maximum ΔT occurs in western Montana (Fig. 2c). (Note:

276 in the interest of brevity, unless otherwise specified, "gradient" refers hereon to a change
277 with respect to a change in horizontal distance x, such as the change in ΔT over some
278 distance: $\Delta(\Delta T)/\Delta x$.) In fall, the primary gradient is from the coast to the interior, though
279 a prominent local maximum occurs in the higher elevations of central Nevada (Fig. 2d).
280 In all seasons, a gradient in ΔT inland from the coast exists, with the strongest gradient
281 occurring in JJA; however, this near-coast gradient in ΔT typically extends only as far
282 inland as the first major mountain range (e.g. Cascades and Sierras).

283 How both T and ΔT vary with topography is partially illustrated in three latitudinal
284 transects through the modeling domain, which are summarized here from west to east: 1)
285 47.75 °N – crosses the Olympics, the Puget Sound, the North Cascades, the Columbia
286 Plateau, the Rockies and ends in the Northern Great Plains, 2) 44 °N – crosses the
287 Oregon Coast Range, the Willamette Valley, the Oregon Cascades, eastern Oregon
288 including the Blue Mountains, the lower Snake River Plain, the Rockies in Idaho, the
289 upper Snake River Plain, and the Rockies in Wyoming, and 3) 37.5 °N – crosses the
290 California Southern Coast Range, the Central Valley, the Sierra Nevada, the Great Basin
291 in Nevada, southern Utah mountain ranges, and the Colorado Plateau.

292 Observed (PRISM) seasonal temperature along with simulated values for each latitudinal
293 transect are shown in Figs. 3 through 6 (left panels). In DJF, MAM, and SON, transect-
294 averaged biases in the historical period range from as small as 0.04 °C (SON; 37.5 °N) to
295 as large as -1.6 °C (DJF; 37.5 °N), and simulated temperatures are within +/-2 °C of
296 PRISM along most of each transect. As such, these differences are of similar magnitudes
297 to the uncertainty in the gridded observational values themselves (Daly et al. 2008).

298 Examples of where the discrepancy exceeds 2 °C in each season are the warm bias over
299 the Columbia Plateau (-120 to -118 °E longitude in panel "a" in Figs. 3-6), the cold bias
300 at the crest of Rockies in Idaho and Wyoming (-115 and -110 °E longitude in panel "c" in
301 Figs. 3-6), and the cold bias on eastern flank of the Sierra Nevada (-118.5 °E longitude in
302 panel "e" in Figs. 3-6). In JJA, the model has a warm bias of 2 to 3 °C (least biased at
303 37.5 °N; most biased at 47.75 °N) with a root mean square error of roughly 3 °C for each
304 transect, and a tendency towards less bias in the mountains. Biases and root mean squared
305 error by season and transect are provided in Table S1 of the Supplementary Material.

306 These biases may partially cancel when examining differences in the simulations of the
307 historical period and future period. However, because many feedbacks are effectively
308 non-linear, the biases can affect the strength of the feedbacks themselves. A clear case of
309 a non-linear relationship is the solid-liquid water phase change and temperature, effecting
310 snowpack dynamics and the snow-albedo feedback. In the case of summer, the warm
311 bias is associated with an underestimate in precipitation over the modeled domain (Li et
312 al., 2015), which may reflect further biases in summer soil moisture, water vapor, and
313 clouds. Given the non-linear relationship between temperature and the saturation
314 pressure of water and evapotranspiration and soil water content, for example, the
315 temperature bias may indicate a source of non-negligible error in the regional temperature
316 change signal. Though we do not assess the influence of bias in this paper, it is an
317 important topic for further investigation.

318 Below we highlight some changes in ΔT along the transects. First, though, we comment
319 on the estimates of 95% confidence intervals in ΔT, which are illustrated by the shading

320 in the right panels of Figs. 3 – 6. The size of the confidence interval using all 100
321 ensemble members (red shading) is on the order of 0.1 °C, meaning that the major spatial
322 patterns shown are primarily responses to the applied forcings and changed boundary
323 conditions, and not simply "noise" from internal variability of the model. For
324 comparison, we also show 95% confidence intervals assuming one (yellow shading) and
325 five (orange shading) ensemble members. For a single ensemble member, the size of the
326 95% confidence interval is about 1°C (consistent with a square root relationship between
327 standard error and sample size). Note that 1°C is about half the domain-averaged
328 simulated difference in ΔT and of similar magnitude to the spatial variability in ΔT across
329 the western US reported here. These confidence intervals illustrate the problem with a
330 typical single-simulation RCM study: the signal may be smaller than the noise.

331 We found that 100 ensemble members were sufficient for our objective of comparing
332 changes in mean temperature at the scale of the model grid cell. An optimal choice of a
333 minimum ensemble size n will depend on a maximum width w of the confidence interval
334 one is willing to accept to meet a given objective. For this study, $n \quad 1/w^2$, where w has
335 units of ºC. However, this relationship is dependent on the particulars of this analysis:
336 e.g., differences in 29-year means of seasonal temperature, a desire to resolve mesoscale
337 variability, and no dynamic feedbacks between the ocean and atmosphere.

338 For DJF, moving from the coast inland towards the first mountain range, there is a
339 positive gradient in ΔT. This pattern is evident in the Olympics and the Oregon and
340 California Coast Ranges (Fig. 3b, d, and f). A positive gradient in ΔT also exists in the
341 upslope direction on the windward side of the second mountain range encountered:

342 Northern and Southern Cascades, and Sierras. However, the local ΔT maxima do not
343 coincide with these second elevation maxima: the ΔT maxima occur partway up the
344 windward slopes of the ranges, with negative gradients in ΔT from the locations of the
345 local maxima in ΔT to the crests of the mountain ranges. This negative gradient in ΔT is
346 more evident in the Southern Cascades and Sierras, where ΔT is ~0.5 °C less at the
347 mountain crest than at the point of local maximum. The dominant ΔT gradients in the
348 western US interior coincide with the Rocky Mountains (Figs. 3b; d), where local ΔT
349 minima also occur in the higher elevations.

350 In MAM, local ΔT maxima do occur at, or near, the elevation maxima in the Olympics
351 (Fig. 4b), Coast Ranges (Fig. 4d) and Cascades (Figs. 4b; d), but not in the higher
352 elevation Sierras (Fig. 4f). Other prominent local ΔT maxima occur on the windward
353 slopes of the Rockies (Fig. 4b; d), but, as with winter, the highest elevations are not the
354 areas of largest ΔT.

355 In JJA, the largest longitudinal gradients in ΔT occur between the coast and first sizable
356 mountain ranges (Fig. 5), after which longitudinal gradients are relatively small. Away
357 from the coast, the dominant gradient in ΔT in JJA is in the latitudinal direction.

358 SON is similar to JJA in that the largest longitudinal gradients occur within a few degrees
359 of the coast (Fig. 6). There is, however, a more positive west-east gradient in the interior
360 during SON than in JJA.

361 **4 Factors Affecting Seasonal and Regional Warming**

It is evident that simulated ΔT varies with elevation across the western US, but the relationship depends on the region and season (Figs. 7 and 8). In winter and spring, the relationship is not monotonic, but rather dome-shaped, with ΔT peaking between roughly 1500 and 2000 m (somewhat higher elevation in the southwest than the northwest US). The summer relationship is also somewhat dome-shaped, though the change in ΔT against elevation is larger for the coastal regions in summer than in winter and spring. In fall, ΔT increases with elevation but largely plateaus at higher elevations. Pepin et al. (2015) provided a review of mechanisms that may lead to differential warming by elevation, or "elevation-dependent warming" as they call it. A number of factors may contribute to the relationships shown here. In particular, we examined the changes in surface albedo, tropospheric lapse rate, precipitation, and surface energy fluxes both spatially and for all seasons. The importance of the climate processes related to these variables depends on the season and location, as discussed below.

4.1 Winter and spring warming

In DJF and MAM, the large gradients in ΔT that occur inland over the first one to three hundred kilometers from the coast are consistent with the land-sea differential warming phenomenon. However, there are also large elevation gradients in this region, so the gradients in ΔT may result from a combination, or interaction, of processes, including snow albedo feedback at higher elevations and changes in the free air lapse rate.

Also in DJF and MAM, the largest ΔT occur at mid-elevation sites, where substantial snow pack is first expected to disappear, pointing to the snow albedo feedback as a

383 dominant control on the spatial pattern of warming. A visual inspection of the spatial
384 pattern of the change in surface albedo (α) in winter and spring indicates substantial
385 spatial coherence between ΔT and $\Delta\alpha$ (compare Fig. 2 with Fig. 9). To estimate the
386 amount of spatial variation in ΔT explained by $\Delta\alpha$, we used ordinary linear least square
387 regression, though by doing so we do not imply that there is a one-way dependency of ΔT
388 on $\Delta\alpha$. We justify using ordinary least squares regression over other regression methods
389 that assume errors on both predictor and predictand (e.g., total least squares) by recalling
390 that our ensemble, though finite, is very large, and therefore we assume that errors in $\Delta\alpha$
391 are small. We excluded grid cells from the linear regression where the decrease in α is
392 less than 0.0002 so the many grid cells with very little to no change in α would not have
393 undue influence on the slope of regression. Note that a correlation with surface albedo
394 could also be due to correlations of changes in albedo and temperature with changes in a
395 third variable, such as cloudiness, rather than solely the albedo feedback. The similarity
396 of the spatial pattern of albedo change (Fig. 9) with the patterns of change in snow water
397 equivalent and change in net downward surface short-wave flux (Figs. S3 and S4,
398 respectively) for winter and spring suggests, however, that the snow albedo feedback is
399 the dominant shortwave feedback.

400 We find strong and significant negative linear relationships between ΔT and $\Delta\alpha$, with $\Delta\alpha$
401 accounting for 19 to 76% of the variance in ΔT, depending on the region and season (Fig.
402 10; Table 1). Though the magnitudes of changes in albedo tend to be smaller in MAM
403 than in DJF, the increase in T for every 0.1 decrease in α is greater in MAM (0.34 to 1.39
404 °C) than in DJF (0.26 to 0.69 °C). This difference in sensitivity between the two seasons

405 is consistent with more short-wave radiation reaching the surface in MAM (snow albedo
406 changes are not a factor when there is no sunlight) because of longer daylight period, and
407 in some regions because of less cloud cover in MAM. Changes in T with decreasing α
408 are also larger west of the Cascades and Sierras than towards the interior; this may be
409 because ΔT gradients west of the Cascades and Sierras are also substantially driven by
410 factors other than changes in α but that are spatially correlated, such as the land-sea
411 warming contrast and changes in cloudiness.

412 Given the simulated sensitivity of ΔT to changes in snowpack, the spatial pattern in ΔT
413 will be strongly influenced by the resolution of the topography and the representation of
414 snow processes in MOSES1. Substantial improvement in fidelity with observations
415 occurs by simply increasing the topographic resolution by decreasing the grid cell size, as
416 simulations using various horizontal resolutions down to 3-4 km demonstrated using the
417 Penn State–NCAR Mesoscale Model (MM5) in the Pacific Northwest US and California
418 (Leung and Qian 2003) and the Weather Research and Forecasting Model (WRF) with
419 the Noah land-surface model in the Sierras (Pavelsky et al. 2011) and Colorado Rockies
420 (Rasmussen et al 2011; Letcher and Minder 2015). The finer grid cell sizes resolve the
421 higher, colder, elevations where the deepest snow accumulates and persists longest, while
422 at coarser resolutions mountain peaks are smoothed. At 25-km resolution, therefore, it is
423 reasonable to speculate that HadRM3P might also generate too little snowpack and
424 deplete it too early in the year in many parts of the western US on the basis of grid cell
425 size alone. Parajka et al. (2010) note that the accuracy of HadRM3P applied over Austria
426 was degraded in areas of high topographic heterogeneity.

427 In addition to resolution limitations, the simplified snow process representation in any
428 land surface model also incurs error in the simulated snowpack dynamics. Among many
429 simplifications, grid surface albedo in MOSES1 is calculated solely as a function of snow
430 depth and surface temperature; for instance, it does not explicitly consider how snow gets
431 "dirty" as it ages with a consequent reduction in albedo (Cox et al. 1999), yet Barlange et
432 al. (2010) found that varying snow albedo over time in the Noah land surface model
433 significantly improved snowpack dynamics. The effect of canopy cover on albedo is also
434 not explicitly simulated; surface albedo is low with dense forest cover once the snow is
435 gone from the canopy, therefore the snow albedo feedback may be overestimated when
436 canopy effects are inadequately represented (e.g. Livneh et al. 2010; Wang et al. 2010).
437 Besides the snow process simplifications and the imperfectly represented terrain, other
438 biases can influence snowpack dynamics. For example, HadAM3P/RM3P shows a cool
439 bias in both winter and spring over mountainous regions in the western US and has a
440 tendency to exaggerate orographic precipitation (Li et al. 2015), both of which would
441 enhance snowpack accumulation. Though a thorough evaluation of snowpack simulation
442 in HadAM3P/RM3P over the western US is beyond the scope of this paper, we do find a
443 general underestimation of snow cover and snow water equivalent, particular in spring in
444 rain-snow transition areas, such as the Oregon Cascades (results not shown here).

445 Large-scale changes in tropospheric lapse rate also influence the relationship between
446 elevation and temperature change. Most of the western US shows a decrease in the
447 simulated free air lapse rate Γ in DJF and MAM between 850 and 500-hPa pressure
448 levels (Figs 11a;b and 12a;b). The sign of the change is consistent with mid-latitude
449 zonal lapse rate projections from GCMs in general when forced with increased

450 greenhouse concentrations (e.g., Fig. 2 in Lorenz and DeWeaver 2007). Changes in Γ
451 range between roughly -0.1 and 0 °C/km, with the largest decreases occurring over
452 western CA. Though these changes in free air lapse rate cannot be directly translated to
453 changes in near surface temperature because of land-surface and atmosphere exchanges
454 (Bradley et al. 2004; Pepin et al. 2015), they do point to the potential for larger
455 temperature increases at high elevations. The changing lapse rates amount to small
456 differences in ΔT (roughly 0.1 °C) between the lowlands and the altitudes of the
457 mountain ranges.

458 *4.2 Summer warming*

459 Unlike winter and spring, the spatial pattern of summer warming is dominated by larger-
460 scale gradients in ΔT (Fig. 2c). To varying degrees the downscaled patterns in all seasons
461 resemble the patterns in the global model output, but JJA (along with SON) shows the
462 most coherence between the global-model and regional-model warming pattern (Fig. S5),
463 suggesting mesoscale variability in processes and feedbacks plays a relatively small role
464 in summer. The relatively large summer warming in the northwest US compared to the
465 southwest US is associated with larger increases in atmospheric pressure in the northwest
466 (see 500-hPa geopotential height changes in Fig. S6), consistent with that region's larger
467 temperature increases and decreased precipitation from suppressed convection.

468 In fact, in the northwest US east of the Cascades, the warming has a similar pattern as
469 that of the changing precipitation P (Fig. 13c). In this region, greater warming generally
470 coincides with larger decreases in P (Fig. 14), where the change in temperature per

relative change in precipitation ($\Delta T/\Delta P$) across space is calculated to be -0.015 °C/% (R^2 = 0.42). Near surface temperature increase can be associated with decreasing precipitation through at least two mechanisms that alter the energy budget (e.g. Seager et al. 2014). The first mechanism is a decrease in cloud cover - for which decreasing precipitation can server as a proxy - permitting more solar radiation to reach, and warm, the surface. In fact, the increase in net downward short-wave flux (Fig. S4c) over the northwestern US points to decrease in cloud cover since summer albedo changes are negligible nearly everywhere. In the second mechanism, a decrease in available soil water (from decreased precipitation) leads to a decrease in surface evaporative cooling and therefore a warming of near-surface air. The greater warming of surface relative to the atmosphere is reflected in the increased upward surface sensible heat at the surface (Fig. S8c) and the associated decrease in upward latent heat flux (Fig. S9c). The similarity in the spatial pattern in the northwest between the changes in precipitation and sensible and latent heat flux is also evident in the change in soil moisture (Fig. S10, panel "c").

Precipitation changes, when considered as a proxy for other processes, can explain about about 0.4 °C of the total range (~1.5 °C) in summer ΔT variation (Fig. 14). However, the association with changing precipitation appears limited to east of the Cascades: no association is apparent in the southwest interior and southern California where summer precipitation is projected to increase (not shown). West of the Cascades, there is also a negative correlation between temperature change and precipitation change, but here the gradients in temperature change owe in part to the proximity to the coast (Fig. 14).

493 Near the coast, much of the range in summer ΔT can still be explained by the differences
494 between land and sea warming, as in other seasons. However, across the southwest US
495 east of the Sierras, there is a large amount of variability in ΔT that we have not associated
496 with any mechanisms or meso-scale landscape features: Here ΔT ranges from about 1.5 to
497 2.3 °C from SE Arizona to NW Nevada, and the changes in precipitation range mostly
498 from near zero to positive. The spatial pattern in summer ΔT shows no apparent
499 connection to precipitation change, nor to changes in the surface radiative energy budget
500 (Figs. S4, S7-S9) or changes in soil moisture (Fig. S10).

501 In contrast to the other seasons, summer's lapse rates increase between the historical and
502 future scenarios over much of the western US (Figs 11c and 12c), though some regions
503 show decreases: western, and some of eastern, Washington and Oregon, and portions of
504 the southwest US. Changes in Γ range between roughly -0.1 and 0.1 °C/km. The largest
505 increases are in the interior regions, particularly the northwest interior, and the largest
506 decreases are in western Washington and Oregon. Interestingly, there is positive
507 relationship between the change in Γ and the historical Γ. We refrain from speculating
508 on the reasons here, but suggest that historical Γ may be used as a diagnostic for
509 understanding the cause of the spatial variability in changing Γ in the simulations.
510 Changes in land-surface fluxes will also influence Γ; an increase in upward surface
511 sensible heat flux in particular may decrease Γ by warming the lower troposphere
512 preferentially. However, the spatial variability of change in Γ does not correspond to
513 changes in sensible heat flux (Fig. S8) in at least two respects: 1) Γ increases over the
514 most of the southwest but the change in upward sensible heat flux is either negative or

largely unchanged over most of this region, and (2) the largest increases in sensible heat flux are west of the Cascades but there Γ decreases.

For the interior regions, increasing lapse rates of the magnitude shown here translate to difference in ΔT of a couple tenths of degree C between the lowland and high mountain elevations in the interior regions, enough to partially explain the slight tendency of decreasing ΔT with elevation seen in Figs. 7c and 8c.

4.3. Fall warming

As with other seasons, during fall the land-sea warming contrast appears to be a primary control on the spatial warming pattern west of the Cascades and Sierras (Fig. 2d). No relationship between the warming pattern and changes in precipitation (Fig. 13d) stands out. Albedo changes (Fig. 9d) are small where present, thus their impacts are also small, and west of the Cascades and Sierras their influence on the positive relationship between ΔT and elevation will be obscured by the coincidental land-sea gradient in ΔT.

Still, in the interior southwest there is a pattern in the warming that bears some relationship to elevation, with an increase in ΔT of about 0.2 °C over a 3 km increase in elevation (Fig. 8d). The largest decreases in free air lapse rate occur during the fall, with decreases exceeding -0.1 °C/km in places (Figs. 11d and 12d). It is possible then that the spatial pattern in fall warming, more than in any other season, shows the imprint of a changing free air lapse rate. As in summer, there is positive correlation between the change in Γ and the historical Γ.

536 *4.4. Comparisons to other studies*

537 There is a limit to what can be learned by comparing previous studies with ours because
538 of a lack of a single experimental design overarching all the studies. Still, it may be
539 possible to make meaningful observations about coarse differences and similarities across
540 results from other mid-21st century seasonal projections that show sufficient spatial detail
541 in the western US.

542 Leung et al. (2004), using PCM/MM5 (40-km resolution), showed stronger winter
543 warming over the coastal mountains (Cascades and Sierra) than elsewhere, which they
544 attributed to snow-albedo feedback effects. They did not report stronger winter warming
545 over the interior mountains, a result they attributed to winter temperature remaining much
546 below freezing even after 1-2.5 °C of warming over the region. This range of warming is
547 similar to our study, though we detect enhanced warming over large portions of the
548 interior where snowpack is depleted.

549 A roughly similar pattern in winter and spring warming is evident in our results and in the
550 CCSM3/WRF (20-km resolution) simulation for the northwest US in Salathé et al.
551 (2010): enhanced warming over the Cascades and flanks of interior mountains, with less
552 warming over the lower elevations of the Columbia Plateau. The ECHAM5/WRF (36-
553 km resolution) winter and spring patterns in Salathé et al. (2010) are markedly different
554 from the CCSM3/WRF patterns, however: the Columbia Plateau shows enhanced
555 warming, and there is no pronounced warming in the Cascades. Salathé et al. (2010)
556 attributed the differences between their two simulations in part to the different boundary
557 conditions coming from the GCMs, though the finer spatial resolution in CCSM4/WRF is

likely also a factor. However, with only a single ensemble member per model, much of these differences may be simply due to internal variability.

The dominant spatial summer warming patterns in Leung et al. (2004), Liang et al. (2006), Salathé et al. (2010), and this study bear little in common with each other, other than they all show less warming near the coast. Though Diffenbaugh et al. (2011) did not present detailed results over the western US, they reported that over the continental US, both the largest warming and largest decreases in precipitation occur in the central US. This pattern of increased warming occurring where there is decreased precipitation is consistent with our results, at least in the northwest US.

Given the dissimilarities in the spatial patterns of summer precipitation changes among the aforementioned studies and the summer relationship of ΔT on ΔP east of the Cascades, it is logical that the summer warming patterns are also very dissimilar in this region. In addition to these few regional modeling studies, projections from GCMs have also not agreed strongly on the sign, much less the magnitude, of summer precipitation change across the western US (Deser et al. 2014; Maloney et al. 2014; Seager et al. 2014). At lead times of about 50 years, much of this "disagreement" arises from internal variability within individual simulations such that the signal-to-noise ratio is low (Hawkins and Sutton 2011); even averaging over ensemble sizes of as large as 40 members from a single GCM model has not shown statistically significant changes over most of the western US (Deser et al. 2014).

While our 100-member ensemble shows a relationship between the warming pattern and precipitation change pattern in the northwest US, the question remains as to how much of this particular precipitation change pattern is a robust response to anthropogenic forcing.

581 Within the confines of the HadAM3P/RM3P framework, this will be explored in a
582 follow-up paper. Answering this question outside of this framework will require large
583 ensembles from a large number of climate models.

584 **5. Conclusions**

585 We report results from the first regional, high-resolution, very-large ensemble, climate
586 model experiment with mid-21st century projections. Our domain is the western US,
587 where the complex terrain induces important spatial variability in warming in response to
588 increased GHGs.

589 Four factors contributing to the spatial pattern in warming over the western US were
590 explored. Though these factors were considered independently, they likely interact. For
591 example, precipitation changes may be driven by changes in the lapse-rate, and the sea-
592 land warming differential is tied to changes in the hydrological cycle and lapse-rates that
593 differ between land and sea. We did not explicitly consider these interactions. The
594 factors are:

595 1) Snow albedo-feedback: The largest control on simulated spatial patterns of warming in
596 winter and spring over much of the western US is the snow-albedo feedback.
597 Consequently, the precise anthropogenic warming patterns shown here will change subtly
598 over time: as the global temperature increases with increasing GHG concentrations, local
599 maxima in ΔT will shift to include areas of progressively higher elevation (e.g. moving
600 from the flanks to the crests of the Rocky Mountains), where large albedo changes are
601 still possible.

2) Temperature-moisture relationship: In summer, we detect a correlation between precipitation change and the magnitude of the warming, particularly over the northwest US interior where the simulations project decreases in summer precipitation. Though decreasing precipitation is not *per se* a direct cause of enhanced warming, it is a proxy for decreasing moisture in the form of soil water content, water vapor, and/or clouds. This relationship poses challenge for attributing a simulated temperature change to anthropogenic forcing because internal variability is high for precipitation, relative to the anthropogenically forced precipitation change. Therefore, we argue for large IC ensembles not just for attributing fine-scale climate model projections in precipitation to applied forcings, but also because of the strong relationship between temperature and precipitation in summer.

3) Tropospheric lapse rate: Changes in free air lapse rates are found to vary spatially and seasonally. In general, decreases and increases (the latter mainly limited to summer) in lapse rate may account for up to a couple of tenths of degree C differences in warming across the western US. These differences are small, but they may explain some of the more subtle features of the relationship of temperature changes with elevation in summer and fall.

4) Sea-land differential warming: In all seasons, the pattern of a warming gradient from the coast to the divides of major north-south mountain ranges (Cascades and Sierras) is consistent with the differential warming between sea and land. The warming in this region also strongly correlates with elevation, but this may be largely happenstance because elevation also increases with distance from coast here. In our simulations, the

624 magnitude of the sea-land differential is partially constrained by the use of prescribed
625 SSTs. More realism would be gained by coupling to a fine-resolution ocean circulation
626 model for the coastal margin, though this would not necessary change the magnitude of
627 warming.

628 Lastly, we recall that western US climate is influenced by large-scale ocean temperature
629 anomaly patterns, particularly in winter, and to a lesser extent in summer. The quantified
630 changes in temperature given here are conditional upon the set of SST and sea ice
631 fraction change patterns applied. Additional simulations with alternate future SSTs and
632 sea ice are needed to assess the sensitivity of the results to the ocean boundary conditions
633 associated with the future forcing scenario.

634

635

Appendix A. Generation of future SSTs

SSTs for the future period were created by adding a change (Δ) in SST to the observed SST in the OSTIA data. The OSTIA data are provided at a 1/20°-resolution so are first regridded to the N96 grid used in HadAM3P.

The ΔSSTs are varied month-by-month and cell-by-cell. The ΔSSTs were derived by differencing SSTs in the future and historic periods as simulated using a coupled atmospheric-ocean GCM. The multiple-step process was as follows:

1. SSTs from the CMIP5 *historical* experiment (1850-2005) were concatenated with those from the CMIP5 *RCP 4.5* experiment (2006-2100).

2. Three-dimensional arrays $\mathbf{X}_i$ (latitude, longitude, time) of monthly SST were generated for the period 1900-2099 for each calendar month i: a total of 12 arrays.

3. $\mathbf{X}_i$ for each i was temporally smoothed using a Gaussian filter along a moving window of 31 years. The standard deviation of weights was scaled to the size the window and was ~5.6 years.

4. ΔSSTs were calculated by subtracting the smoothed SSTs for the period December 1985 to November 2014 from the smoothed SSTs for the period December 2030 to November 2059 (e.g. November 2030 minus December 1985).

5. ΔSSTs were regridded to the N96 grid used in HadAM3P.

6. ΔSSTs were interpolated over land to avoid coastline mismatch between HadAM3P and the CMIP5 GCM, and the HadAM3P land mask was applied.

7. ΔSSTs were spatially smoothed using a Gaussian filter.

8. ΔSSTs were added to the regridded OSTIA SSTs for the period December 1985 to November 2014 to derive SSTs for the period December 2030 to November 2059.11.

Appendix B. Model spin-up

The strength of Weather@home is its ability to generate very large ensemble of short runs (e.g. one-year long) relatively quickly. A compromise for this strength is that runs of many consecutive years (as typically done during spin-up) are cumbersome. The spin-up procedure described below arose out of a need to balance available resources with efficacy while operating with the Weather@home structure; in other words, to avoid continuous, multi-decadal spin-up runs.

For the historical scenario, the spin-up began with an existing single 10-year long continuous simulation ending in 1967.11 (see Massey et al. 2014). The final model state state from this run, saved in a "restart" file, was then used to provide the initial conditions for each of 28 single-year runs beginning in December of the years 1985 through 2012 and ending November 1986 through 2013. Next, the restart files from each of these 28 simulations were used as the initial conditions of single-year simulations beginning in December of the years 1986-2013. The restart file from 1986.11 was used to initialize 1985.12 because there was no simulation ending in 1985.11.

For the future, a historical run, spun-up using the above method, seeded the spin-up procedure: a restart file from 2011.11 was used to initialize single-year simulations beginning 2030.12, 2035.12, 2040.12, 2045.12, 2050.12, and 2055.12. Next, the restart files for each of these 6 runs initialized at least four single-year runs in consecutive years. For example, the restart file for 2031.11 initialized 2030.12, 2031.12, 2032.12, 2033.12, 2034.12, and 2035.12, while the 2036.11 restart file initialized 2036.12, 2037.12, 2038.12, 2039.12, and 2040.12. Lastly, the restart files from each of these 28 simulations ending in 2030.11 through 2057.11 were used as the initial conditions of single-year simulations beginning in December of the years 2031-2057. The new restart file from 2031.11 was also used to initialize 2030.12 because there was no simulation ending in 2030.11. In summary, each modeled year in the future scenario underwent 15 years of spin-up, of which the last 3 spin-up years were driven by the forcings and boundary conditions of the year's respective time period under *RCP 4.5*.

Acknowledgements

The work was supported in part by the U.S. Department of Agriculture, National Institute of Food and Agriculture (USDA-NIFA), via the Regional Approaches to Climate Change – Pacific Northwest Agriculture (REACCH PNA, USDA-NIFA grant 2011068002-30191) project and USDA-NIFA grant 2013-67003-20652, and Sihan Li was funded through a Department of the Interior Northwest Climate Science Center graduate fellowship. The authors thank Andy Bowery, Friederike Otto, and the entire team at Weather@home for their assistance and the thousands of volunteers who supplied computing power for this study, and also thank Richard Betts from the UK Met Office

696 Hadley Centre and William Ingram from University of Oxford for their expert
697 consultation. Weather@home uses The Berkeley Open Infrastructure for Network
698 Computing (BOINC), which is supported by the National Science Foundation through
699 awards SCI-0221529, SCI-0438443, SCI-0506411, PHY/0555655, and OCI-0721124.
700 The data used for this paper are available by request from the corresponding author.

701

References

Barlage M, et al (2010) Noah land surface model modifications to improve snowpack prediction in the Colorado Rocky Mountains. J Geophys Res 115: D22101. doi:10.1029/2009JD013470

Bradley RS, Keimig FT, Diaz HF (2004) Projected temperature changes along the American cordillera and the planned GCOS network. Geophys Res Lett 31: L16210. doi:10.1029/2004GL020229.

Boulanger JP, et al (2010) A Europe-South America network for climate change assessment and impact studies. Clim Change 98: 307-329. doi:10.1007/s10584-009-9734-8

Christensen JH, Christensen OB (2007) A summary of the PRUDENCE model projections of changes in European climate by the end of the century. Clim Change 81: 7–30. doi:10.1007/s10584-006-9210-7

Cox PM, Betts RA, Bunton CB, Essery RLH, Rowntree PR, Smith J (1999) The impact of new land surface physics on the GCM simulation of climate and climate sensitivity. Clim Dyn 15:183-203

Daly C, Halbleib MD, Smith JI, Gibson WP, Doggett MK, Taylor GH, Curtis J, Pasteris PA (2008) Physiographically-sensitive mapping of temperature and precipitation across the conterminous United States. Int J Climatol 28: 2031-2064. doi:10.1002/joc.1688

Daly C, Conklin DR, Unsworth MH (2010) Local atmospheric decoupling in complex topography alters climate change impacts. Int J Climatol, 30: 1857–1864. doi: 10.1002/joc.2007

Deser C, Philips AS, Bourdette V, Teng H (2012) Uncertainty in climate change projections: The role of internal variability. Clim Dyn 38: 527-546. doi:10.1007/s00382-010-0977-x

Deser C, Phillips AS, Alexander MA, Smoliak BV (2014) Projecting North American climate over the next 50 Years: Uncertainty due to internal variability. J Clim 27: 2271-2296, doi:10.1175/JCLI-D-13-00451.1

Diffenbaugh NS, Pal JS, Trapp RJ, Giorgi F (2005) Fine-scale processes regulate the response of extreme events to global climate change. Proc Natl Acad Sci 102:15774–15778. doi:10.1073/pnas.0506042102

Diffenbaugh NS, Ashfaq M, Scherer M (2011) Transient regional climate change: analysis of the summer climate response in a high-resolution, century-scale

736 ensemble experiment over the continental United States. J Geophys Res Atmos
737 116:1–16. doi:10.1029/2011JD016458

738 Donlon CJ, Martin M, Stark J, Roberts-Jones J, Fiedler E, Wimmer W (2012) The
739 operational sea surface temperature and sea ice analysis (OSTIA) system. Remote
740 Sens Environ 116: 140-158. doi:10.1016/j.rse.2010.10.017

741 Duffy PB, Arritt RW, Coquard J, Gutowski W, Han J, Iorio J, Kim J, Leung LR, Roads J,
742 Zeledon E (2006) Simulations of present and future climates in the western
743 United States with four nested regional climate models. J Clim 19: 873–895.
744 doi:10.1175/JCLI3669.1

745 Dulière V, Zhang Y, Salathé Jr EP (2011) Extreme precipitation and temperature over the
746 U.S. Pacific Northwest: a comparison between observations, reanalysis data, and
747 regional models. J Clim 24: 1950-1964

748 Dulière V, Zhang Y, Salathé Jr EP (2013) Changes in twentieth-century extreme
749 temperature and precipitation over the western United States based on
750 observations and regional climate model simulations. J Clim 26: 8556–8575.
751 doi:10.1175/JCLI-D-12-00818.1

752 Giorgi F, Hurrell JW, Marinucci MR, Beniston M (1997) Elevation dependency of the
753 surface climate change signal: A model study. J Clim 10: 288–296

754 Giorgi F, Brodeur CS, Bates GT (1994) Regional climate change scenarios over the
755 United States produced with a nested regional climate model. J Clim 7: 375–399

756 Hawkins E, Sutton R (2009) The potential to narrow uncertainty in regional climate
757 predictions. Bull Am Meteorol Soc 90: 1095-1107.
758 doi:10.1175/2009BAMS2607.1

759 Hawkins E, Sutton R (2011) The potential to narrow uncertainty in projections of
760 regional precipitation change. Clim Dyn 37: 407-418. doi: 10.1007/s00382-010-
761 0810-6

762 Hostetler SW, Alder JR, Allan AM (2011) Dynamically downscaled climate simulations
763 over North America: Methods, evaluation, and supporting documentation for
764 users: U.S. Geological Survey Open-File Report 2011-1238. 64 p.

765 Joshi MM, Gregory JM, Webb MJ, Sexton DM, Johns TC (2008) Mechanisms for the
766 land/sea warming contrast exhibited by simulations of climate change. Clim Dyn
767 5: 455-465.

768 Kotlarski S, Bosshard T, Lüthi D, Pall P, Schär C (2012). Elevation gradients of
769 European climate change in the regional climate model COSMO-CLM. Clim
770 Change 112: 189-215. doi:10.1007/s10584-011-0195-5

771 Li S, Mote PW, Rupp DE, Vickers D, Mera R, Allen MR (2015) Evaluation of a regional
772 climate modeling effort for the western United States using a superensemble from
773 weather@home. J Clim 28: 7470-7488. doi: 10.1175/JCLI-D-14-00808.1

774 Liang, X-Z, Pan J, Zhu J, Kunkel KE, Wang JXL, Dai A (2006) Regional climate model
775 downscaling of the U.S. summer climate and future change, J Geophys Res 111:
776 D10108. doi:10.1029/2005JD006685

777 Letcher TW, Minder JR (2015) Characterization of the simulated regional snow albedo
778 feedback using a regional climate model over complex terrain. J Clim 28: 7576–
779 7595. doi: 10.1175/JCLI-D-15-0166.1

780 Leung LR, Ghan SJ, (1999) Pacific Northwest climate sensitivity simulated by a regional
781 climate model driven by a GCM. Part II: $2\times CO_2$ simulations. J Clim 12: 2031–
782 2053

783 Leung LR, Qian Y (2003) The sensitivity of precipitation and snowpack simulations to
784 model resolution via nesting in regions of complex terrain. J Hydrometeor 4:
785 1025–1043

786 Leung LR, Qian Y, Bian X, Washington WM, Han J, Roads JO (2004) Mid-century
787 ensemble regional climate change scenarios for the western United States. Clim
788 Change 62: 75-113. doi:10.1023/B:CLIM.0000013692.50640.55

789 Livneh B, Xia Y, Mitchell KE, Ek MB, Lettenmaier DP (2010) Noah LSM snow model
790 diagnostics and enhancements. J Hydrometeor 11: 721-738. doi:
791 10.1175/2009JHM1174.1

792 Lorenz, EN (1963) Deterministic nonperiodic flow. J Atmos Sci 20: 130–141.

793 Lorenz DJ, DeWeaver ET (2007) Tropopause height and zonal wind response to global
794 warming in the IPCC scenario integrations. J Geophys Res 112: D10119. doi:
795 10.1029/2006JD008087.

796 Mahoney K, Alexander M, Scott JD, Barsugli J (2013) High-resolution downscaled
797 simulations of warm-season extreme precipitation events in the Colorado Front
798 Range under past and future climates. J Clim 26: 8671–8689. doi:10.1175/JCLI-
799 D-12-00744.1

800 Maloney ED, et al. (2014) North American climate in cmip5 experiments: part iii:
801 assessment of twenty-first-century projections. J Clim 27: 2230-2270. doi:
802 10.1175/JCLI-D-13-00273.1

803 Massey N, Jones R, Otto FEL, Aina T, Wilson S, Murphy JM, Hassel D, Yamazaki YH,
804 Allen MR (2014) weather@home – development and validation of a very large

805 ensemble modelling system for probabilistic event attribution. Q J R Meteorol
806 Soc. doi:10.1002/qj.2455

807 Mearns LO, et al (2013) Climate change projections of the North American regional
808 climate change assessment program (NARCCAP). Clim Change 120: 965-975.
809 doi:10.1007/s10584-013-0831-3

810 Meehl GA, Washington WM, Arblaster JM, Hu A, Teng H, Kay JE, Gettelman A,
811 Lawrence DM, Sanderson BM, Strand WG (2013) Climate change projections in
812 CESM1(CAM5) compared to CCSM4. J Clim 26: 6287–6308. doi:10.1175/JCLI-
813 D-12-00572.1

814 Meinshausen M, et al (2011) The RCP greenhouse gas concentrations and their
815 extensions from 1765 to 2300. Clim Change 109: 213–241. doi:10.1007/s10584-
816 011-0156-z

817 Mesinger MJ, et al (2006) North American Regional Reanalysis. Bull Amer Meteor Soc
818 90: 993-1007. doi:10.1175/BAMS-87-3-343

819 Mote PW, Allen MR, Jones RG, Li S, Mera R, Rupp DE, Salahuddin A, Vickers D
820 (2015) Superensemble regional climate modeling for the western US, Bull Am
821 Meteorol Soc. doi:10.1175/BAMS-D-14-00090.1

822 O'Brien TA, Sloan LC, Snyder MA (2011) Can ensembles of regional climate model
823 simulations improve results from sensitivity studies? Clim Dyn 37:1111−1118.
824 doi:10.1007/s00382-010-0900-5

825 Parajka J, Dadson S, Lafon T, Essery R (2010) Evaluation of snow cover and depth
826 simulated by a land surface model using detailed regional snow observations from
827 Austria. J Geophys Res Atmos 115: D24117. doi:10.1029/2010JD014086

828 Pavelsky TM, Kapnick S, Hall A (2011) Accumulation and melt dynamics of snowpack
829 from a multiresolution regional climate model in the central Sierra Nevada,
830 California. J Geophys Res Atmos 116: D16115. doi:10.1029/2010JD015479

831 Pavelsky TM, Sobolowski S, Kapnick S, Barnes JB (2012) Changes in orographic
832 precipitation patterns caused by a shift from snow to rain. Geophys Res Lett 39:
833 L18706. doi:10.1029/2012GL052741

834 Pepin N, et al (2015) Elevation-dependent warming in mountain regions of the world.
835 Nature Clim Change 5: 424-430. doi:10.1038/nclimate2563

836 Plummer DA, Caya D, Frigon A, Côté H, Giguère M, Paquin D, Biner S, Harvey R, de
837 Elia R (2006): Climate and climate change over North America as simulated by
838 the Canadian RCM. J Clim 19: 3112–3132. doi:10.1175/JCLI3769.1

839 Ramanathan V, Lian MS, Cess RD (1979) Increased atmospheric CO_2: Zonal and
840 seasonal estimates of the effect on the radiation energy balance and surface
841 temperature. J Geophys Res 84(C8): 4949–4958. doi:10.1029/JC084iC08p04949

842 Rasmussen R, et al (2011) High-resolution coupled climate runoff simulations of
843 seasonal snowfall over Colorado: A process study of current and warmer climate.
844 J Clim 24: 3015–3048. doi: 10.1175/2010JCLI3985.1

845 Rupp DE, Abatzoglou JT, Hegewisch KC, Mote PW (2013) Evaluation of CMIP5 20th
846 century climate simulations for the Pacific Northwest USA. J Geophys Res Atmos
847 118: 10884–10906. doi:10.1002/jgrd.50843

848 Salathé Jr EP, Steed R, Mass CF, Zahn P (2008) A high-resolution climate model for the
849 United States Pacific Northwest: Mesoscale feedbacks and local responses to
850 climate change. J Clim 21: 5708–5726

851 Salathé Jr EP, Leung LR, Qian Y, Zhang Y (2010) Regional climate model projections
852 for the State of Washington. Clim Change 102: 51-75. doi:10.1007/s10584-010-
853 9849-y

854 Seager R, Goddard L, Nakamura J, Henderson N, Lee DE (2014) Dynamical causes of
855 the 2010/11 Texas-Northern Mexican drought. J Hydrometeor 15: 39-68.
856 doi:10.1175/JHM-D-13-024.1

857 Seager R, Neelin D, Simpson I, Liu H, Henderson N, Shaw T, Kushnir Y, Ting M, Cook
858 B (2014) Dynamical and thermodynamical causes of large-scale changes in the
859 hydrological cycle over North America in response to global warming. J Clim 27:
860 7921-7948. doi: 10.1175/JCLI-D-14-00153.1

861 Šeparović L, Alexandru A, Laprise R, Martynov A, Sushama L, Winger K, Tete K, Valin
862 M (2013) Present climate and climate change over North America as simulated by
863 the fifth-generation Canadian regional climate model. Clim Dyn 41: 3167-3201.
864 doi:10.1007/s00382-013-1737-5

865 Sheffield J, et al (2013) North American climate in CMIP5 experiments. Part 1:
866 Evaluation of historical simulations of continental and regional climatology. J
867 Clim 26: 9209-9245. doi:10.1175/JCLI-D-12-00592.1

868 Sutton RT, Dong B, Gregory JM (2007) Land/sea warming ratio in response to climate
869 change: IPCC AR4 model results and comparison with observations. Geophys
870 Res Lett 34: L02701, doi:10.1029/2006GL028164

871 Taylor KE, Stouffer RJ, Meehl GA (2012) An overview of CMIP5 and the experiment
872 design. Bull Am Meteorol Soc 93: 485–498. doi:10.1175/BAMS-D 11-973
873 00094.1

van der Linden P, Mitchell JFB (2009) ENSEMBLES: Climate change and its impacts: Summary of research and results from the ENSEMBLES project, technical report, Met Off. Hadley Cent., Exeter, U. K.

Wang C, Jones R, Perry M, Johnson C, Clark P (2013) Using an ultrahigh-resolution regional climate model to predict local climatology. QJR Meteorol Soc 139: 1964–1976. doi: 10.1002/qj.2081

Wang J, Kotamarthi VR (2015) High-resolution dynamically downscaled projections of precipitation in the mid and late 21st century over North America. Earth's Future 3: 268-288. doi:10.1002/2015EF000304

Wang Z, Zeng X, Decker M (2010) Improving snow processes in the Noah land model. J Geophys Res Solid Earth 115: D20108. doi:10.1029/2009JD013761

Zhang Y, Dulière V, Mote P, Salathé Jr EP (2009) Evaluation of WRF and HadRM mesoscale climate simulations over the United States Pacific Northwest. J Clim 22: 5511– 5526

889
890

Table 1. Slope of the linear relationship between the change in temperature (T) and the decrease in albedo (α) given as the change in T for a -0.1 change in α from the historical period to the future scenario for $\Delta\alpha < -0.0002$.

Region	Winter (DJF)			Spring (MAM)		
	$-0.1\Delta T/\Delta\alpha$ (°C)	Inner 95% C.I.	R^2	$-0.1\Delta T/\Delta\alpha$ (°C)	Inner 95% C.I.	R^2
Western WA/OR	0.55	0.49, 0.60	0.51	1.39	1.24, 1.55	0.76
Eastern WA/OR	0.26	0.23, 0.30	0.32	0.80	0.72, 0.88	0.55
Northwest Interior	0.54	0.51, 0.57	0.68	0.38	0.33, 0.42	0.24
Western CA	0.69	0.55, 0.83	0.41	1.25	1.08, 1.41	0.70
Southwest Interior[1]	0.30	0.28, 0.32	0.32	0.34	0.30, 0.39	0.19

[1]Merged with eastern CA

891

892
893

894

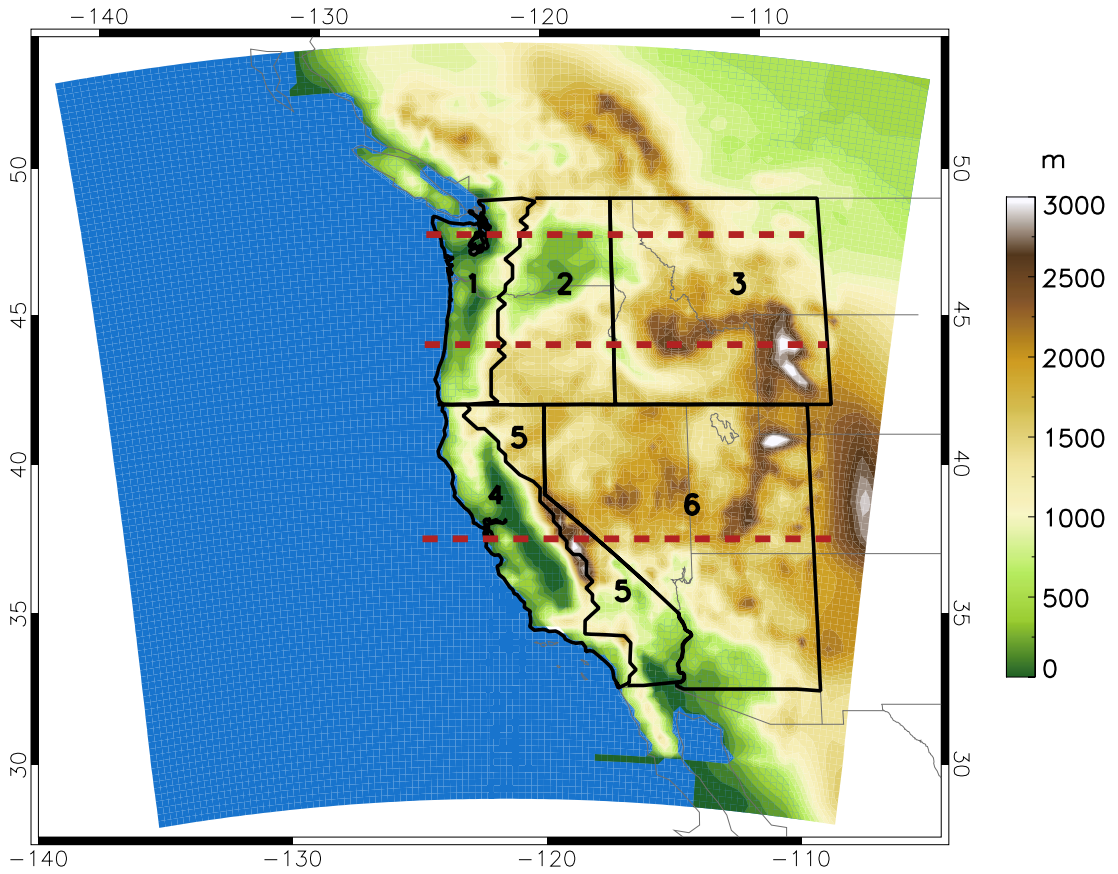

895

896 **Figure 1.** Domain of HadRM3P with surface elevation. Red dashed lines show the
897 latitudinal transects discussed in the text. Dark lines bound the sub-domains: 1) Oregon
898 and Washington west of, and including, the Cascade Range divide (Western OR/WA); 2)
899 Oregon and Washington east of the Cascade divide (Eastern OR/WA); 3) Idaho, Montana
900 and Wyoming north of 42°N and west of 108°W (Northwest interior); 4) California west
901 of the Sierra Nevada and Cascade Range divides (Western CA); 5) California east of the
902 Sierra Nevada and Cascade Range divides (Eastern CA); 6) Nevada, Utah, and Arizona
903 north of 32.5°N, including the southwest corner of Wyoming (Southwest interior).

904

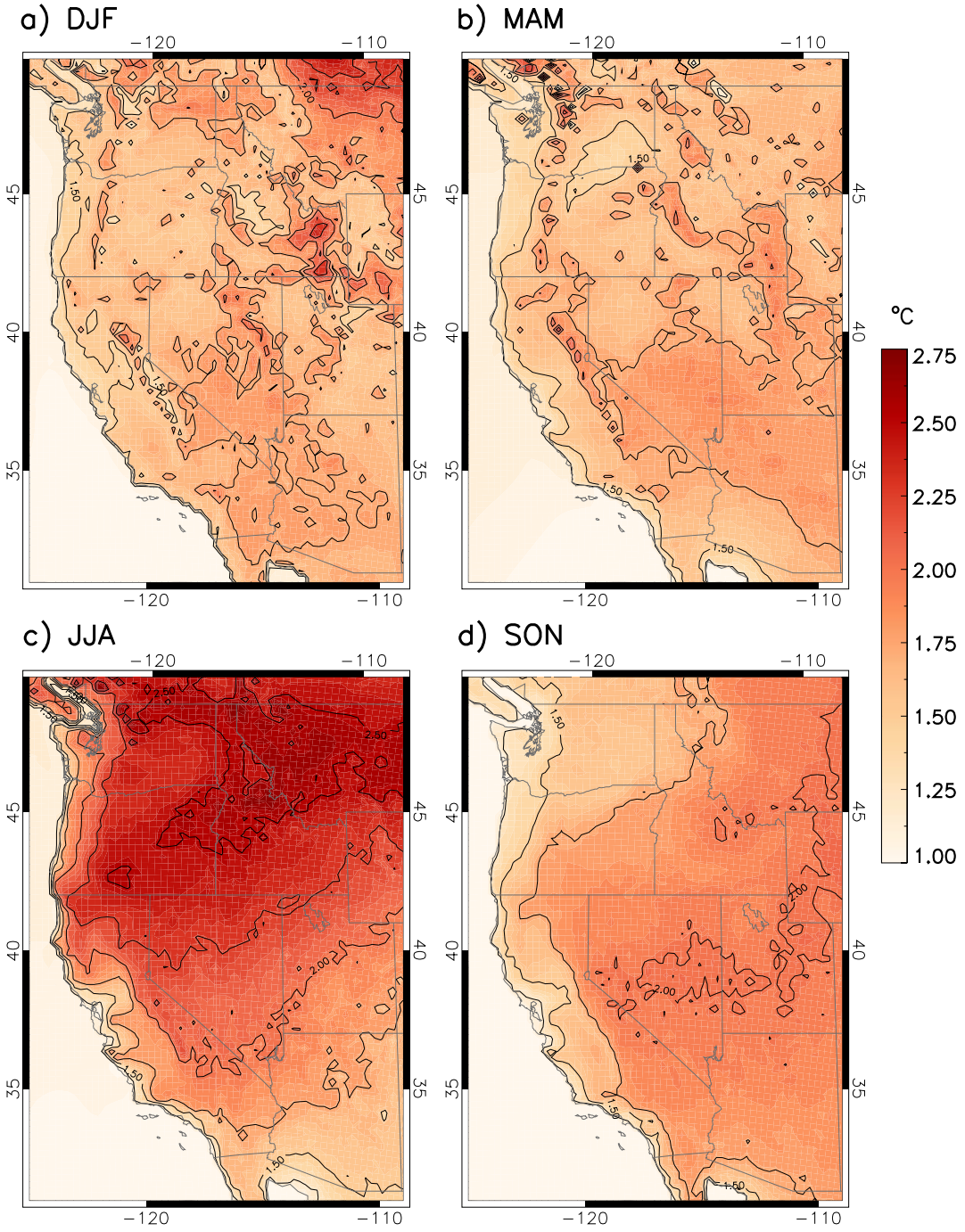

Figure 2. Change in ensemble mean seasonal mean 2-m air temperature (ΔT) from the historical period (Dec. 1985 – Nov. 2014 to the future scenario (Dec. 1985 – Nov. 2014; *RCP 4.5*) for a) winter (DJF), b) spring (MAM), c) summer (JJA), and d) fall (SON). Values are averaged over all 100 ensemble members per year and over all 29 years per period for each model grid point. Contour intervals for lines are 0.25°C.

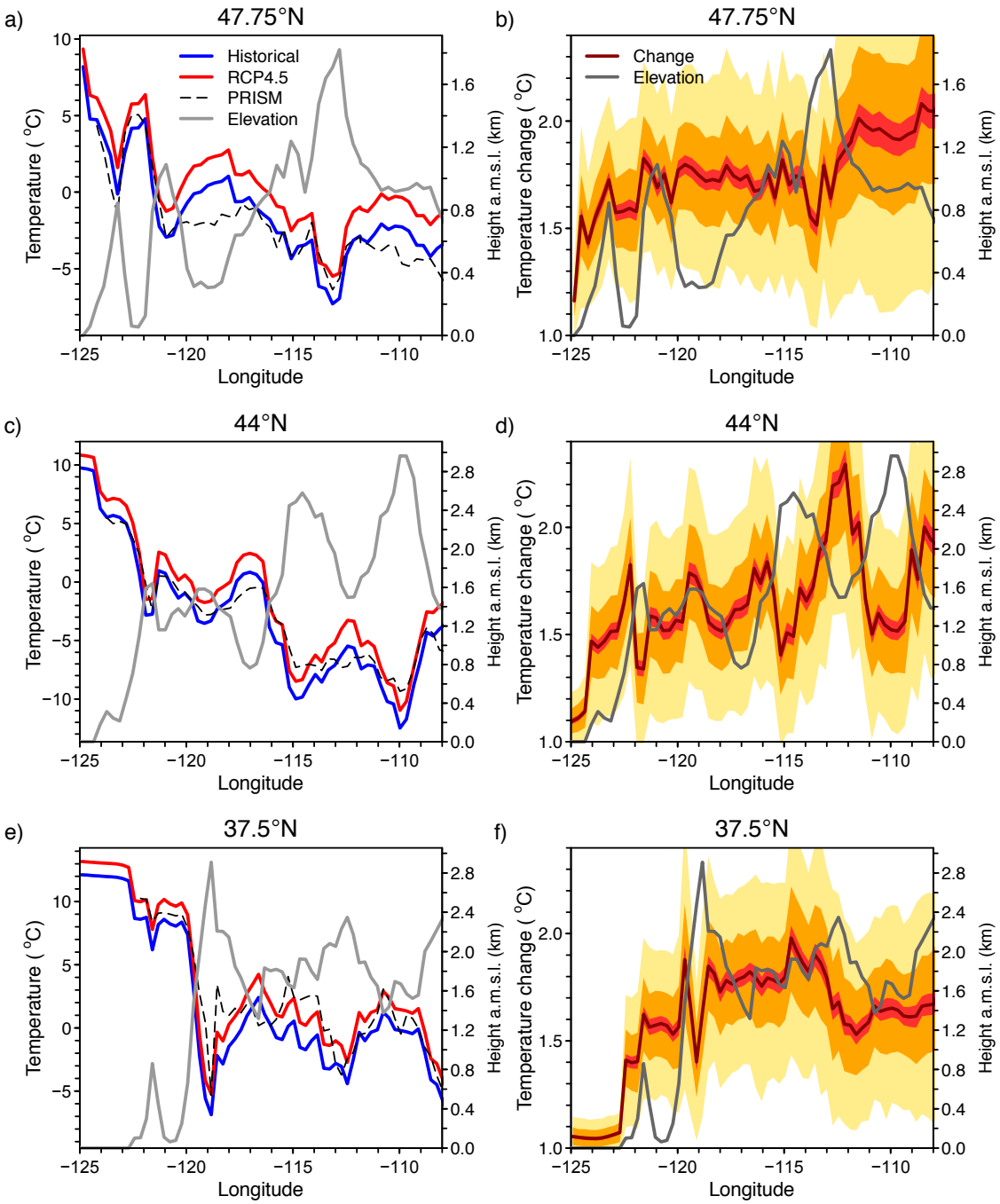

Figure 3. Ensemble mean winter (DJF) near surface (1.5 m) air temperature for the historical period and future (*RCP 4.5*) scenario along three longitudinal transects (left column) and the change from the historical period to the future scenario along the same three longitudinal transects (right column). Yellow, orange, and red shading show the 95% confidence intervals using 1, 5, and 100 ensemble members per year, respectively. Also shown are the historical data from PRISM (dashed lines, left) and elevation (grey)

920 along each transect. Note that the mean temperature and elevation y-axis ranges differ for
921 each transect.

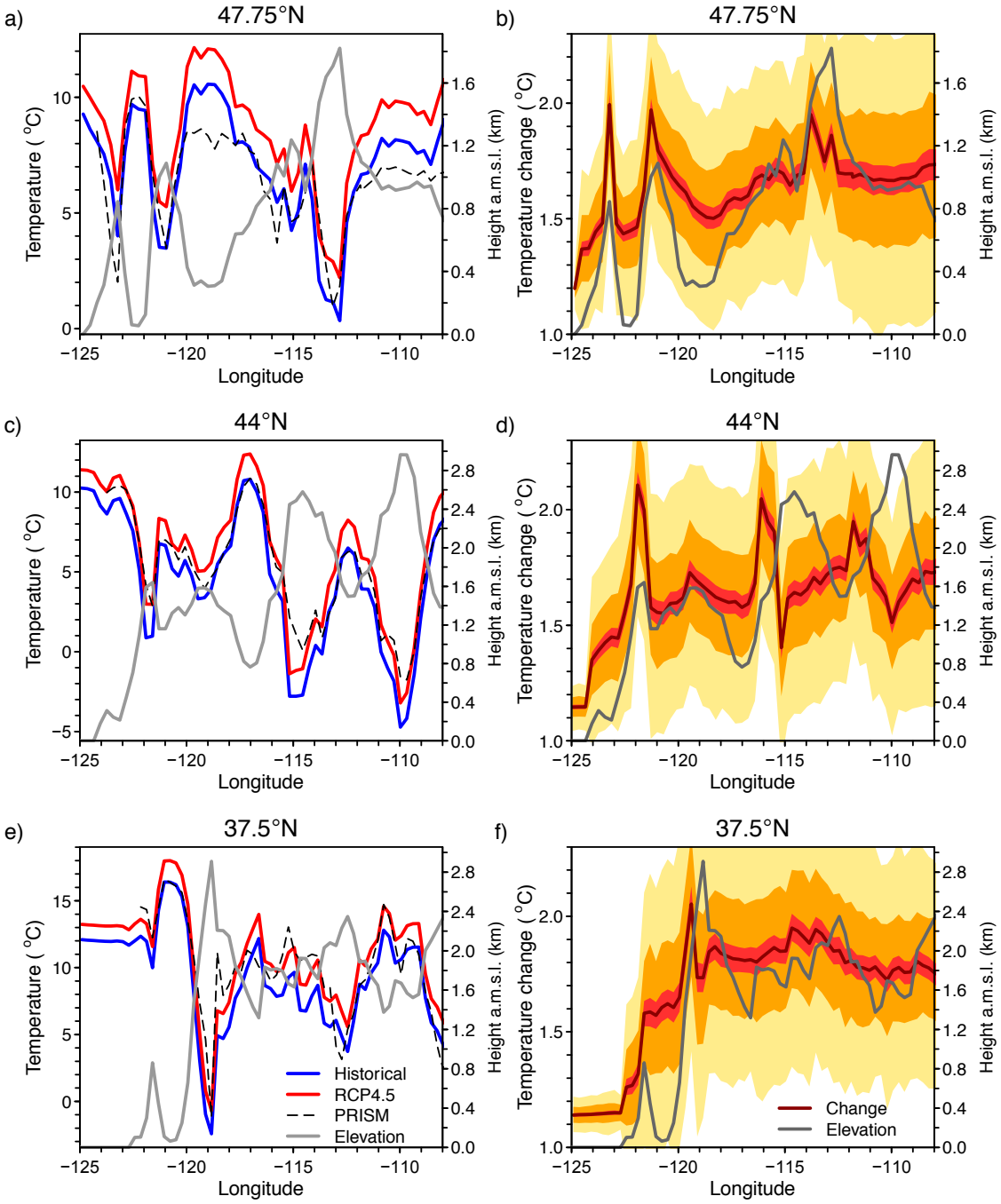

Figure 4. As Fig. 3 but for spring (MAM). Note that mean temperature and temperature change y-axis ranges differ from those in Fig. 3.

927

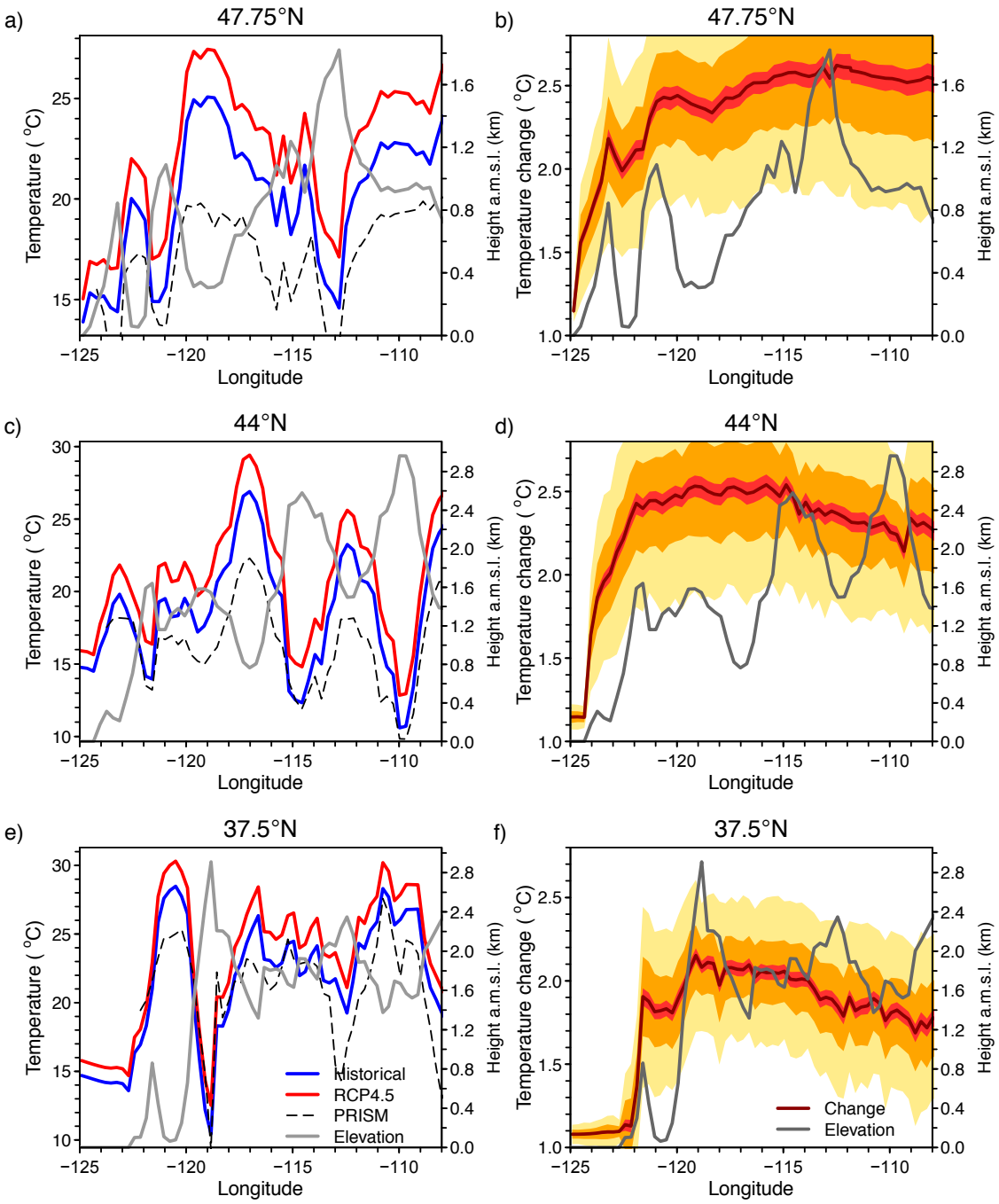

928

929 **Figure 5.** As Fig. 3 but for summer (JJA). Note that mean temperature and temperature
930 change y-axis ranges differ from those in Fig. 3.

931

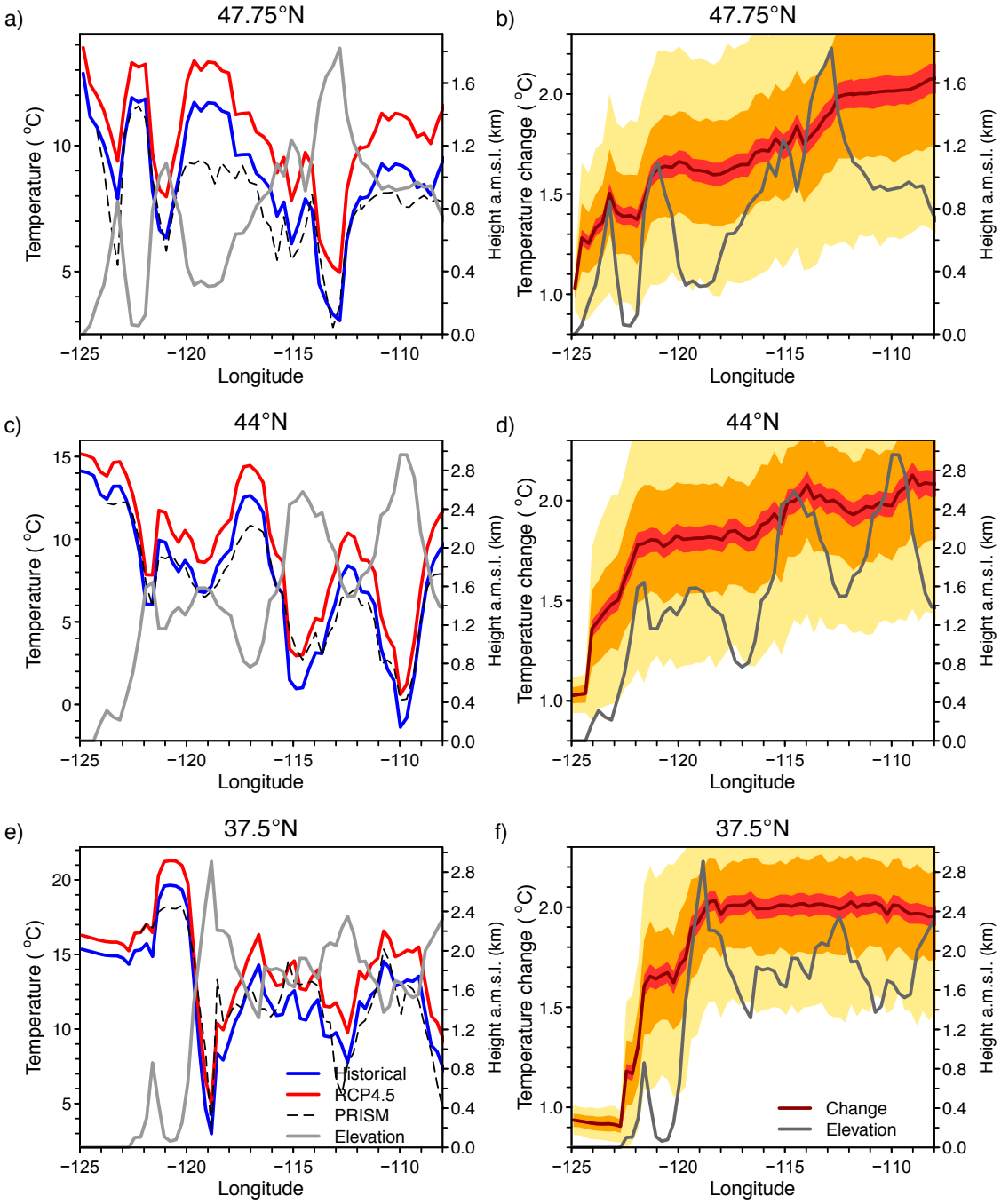

Figure 6. As Fig. 3 but for fall (SON). Note that mean temperature and temperature change y-axis ranges differ from those in Fig. 3.

937

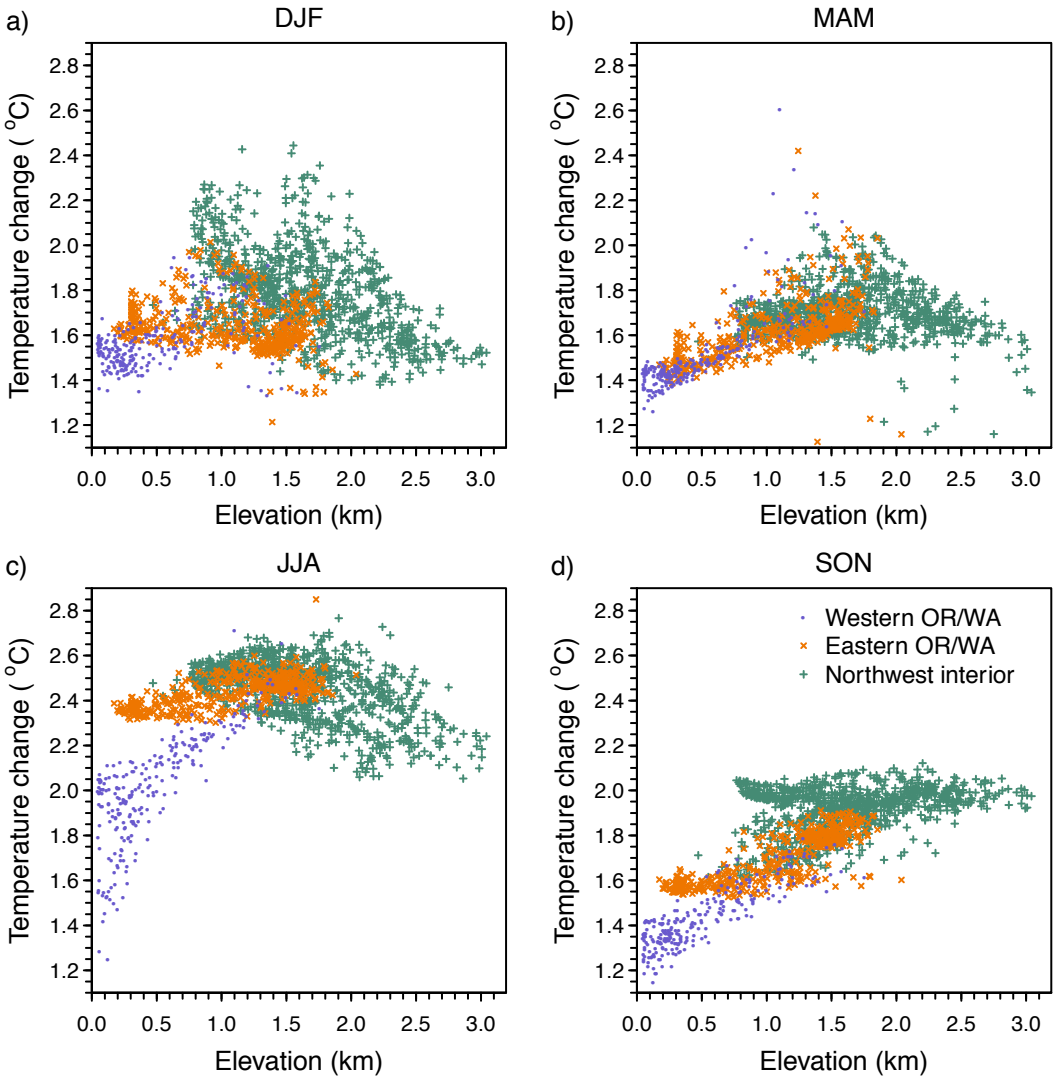

938

939 **Figure 7.** Change in ensemble mean a) winter (DJF), b) spring (MAM), c) summer (JJA),
940 and d) fall (SON) near surface air temperature from the historical period to the future
941 scenario against elevation in the northwestern US. One point is shown for each model
942 grid cell. Symbols are colored by sub-domain (see Fig. 1).

943

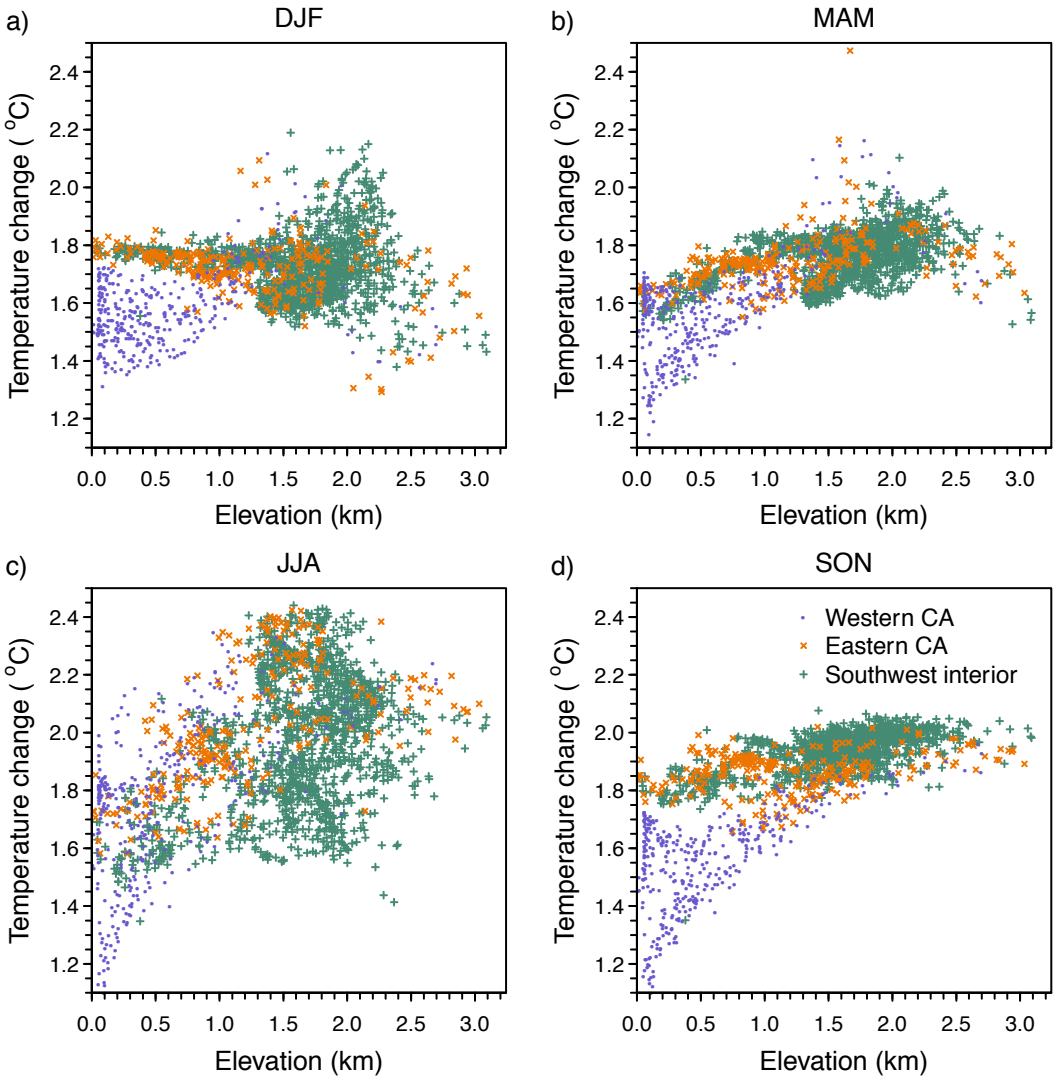

Figure 8. Same as Fig. 7 but for the southwestern US. Note the y-axis ranges differ from Fig. 7.

950

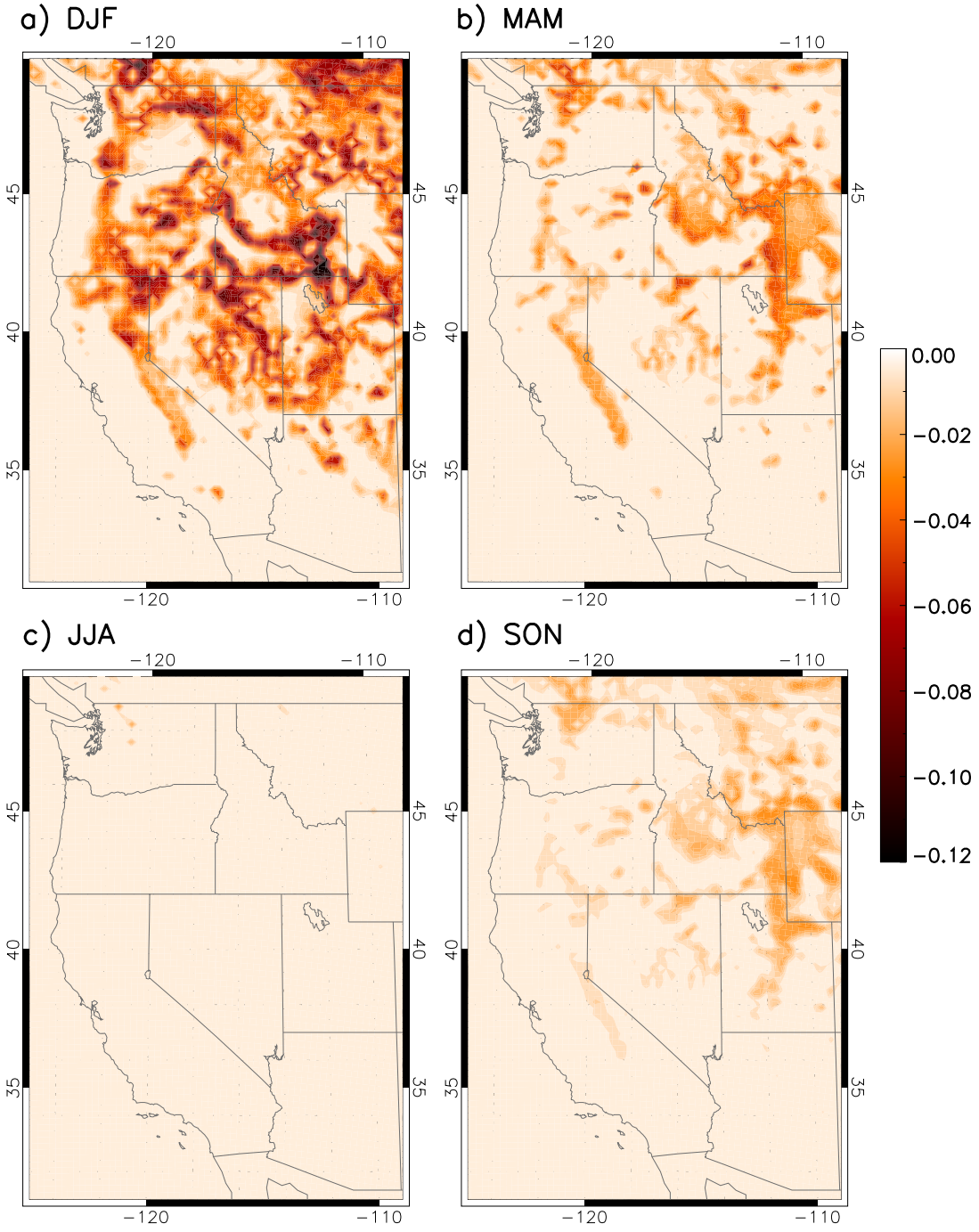

951

952 **Figure 9.** Change in ensemble mean a) winter (DJF), b) spring (MAM), c) summer (JJA),
953 and d) fall (SON) mean surface albedo from the historical period to the future scenario.

954

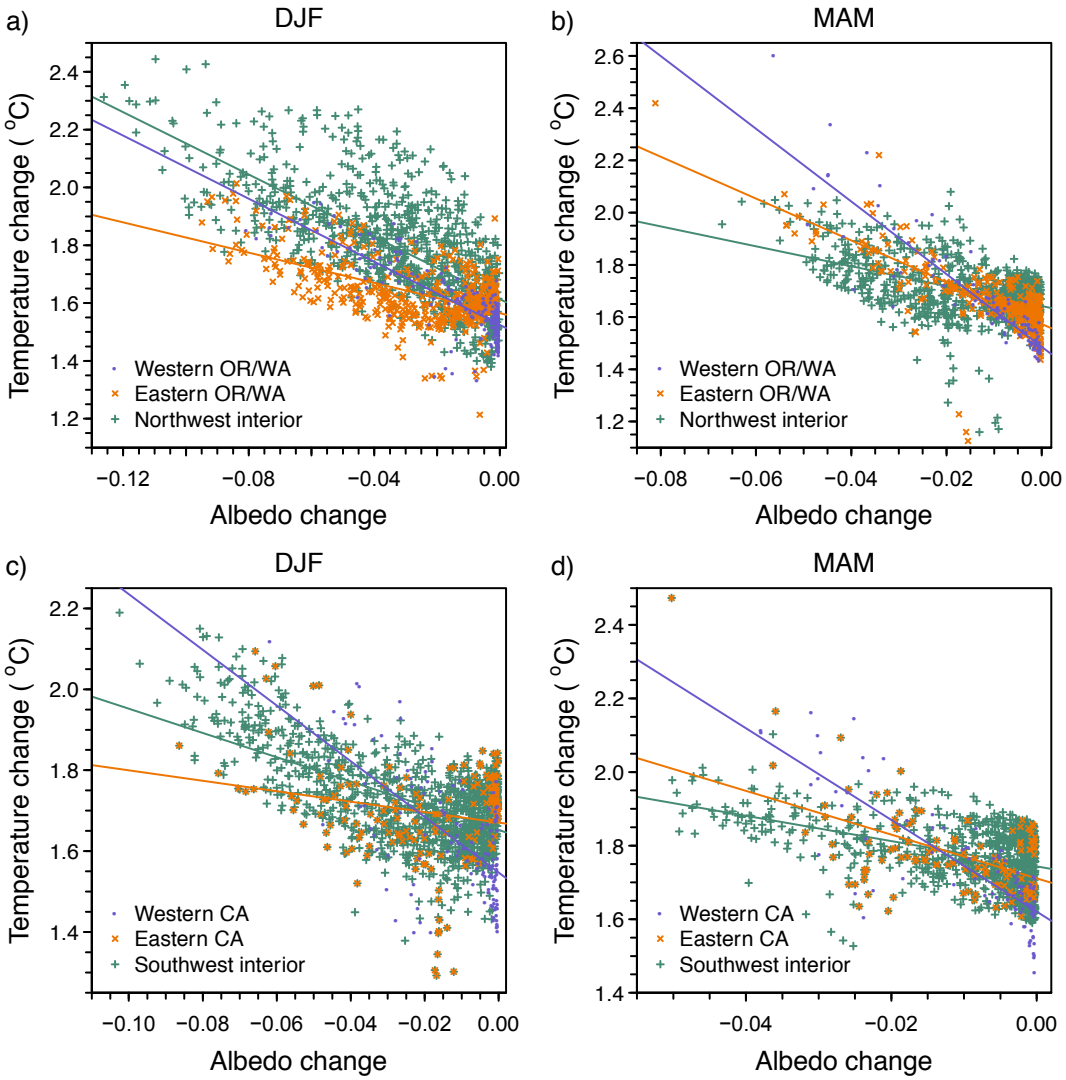

Figure 10. Change in ensemble mean winter (DJF, left) and spring (MAM, right) seasonal air temperature against change in albedo from the historical to the future scenario for the northern (top) and southern (bottom) regions. One point is shown for each model grid cell with change in albedo < -0.002. Symbols are colored by sub-domain (see Fig. 1). Lines show fit of linear model by regions. Note the y-axes ranges differ among panels.

964

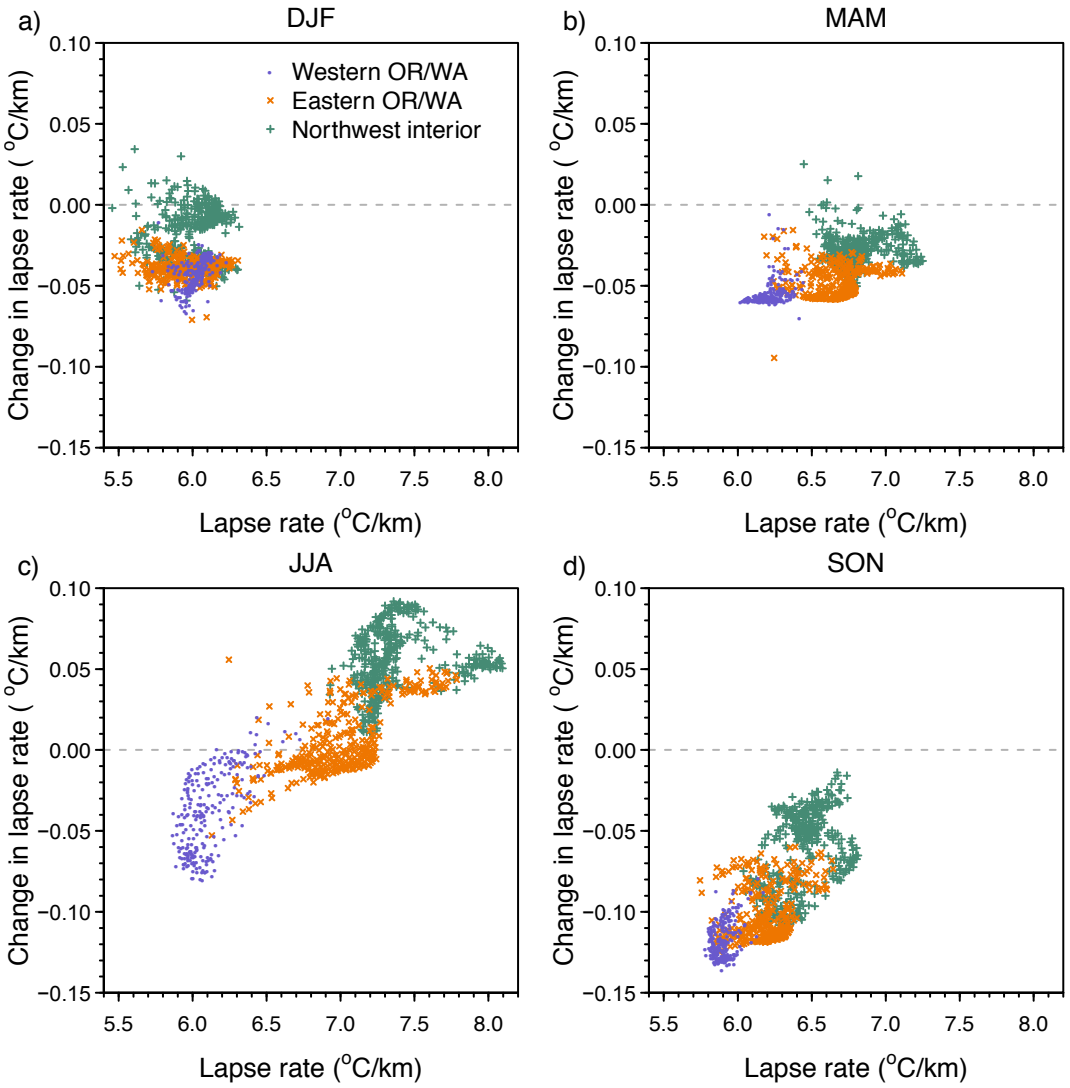

965

966 **Figure 11.** Change in ensemble mean a) winter (DJF), b) spring (MAM), c) summer
967 (JJA), and d) fall (SON) lapse rate, $\Gamma = -dT/dz$, between 850-hPa and 500-hPa
968 geopotential heights from the historical to the future scenario against mean lapse rate for
969 the historical period in the northwestern US. One point is shown for each model grid
970 cell. Symbols are colored by sub-domain (see Fig. 1).

971

972

973

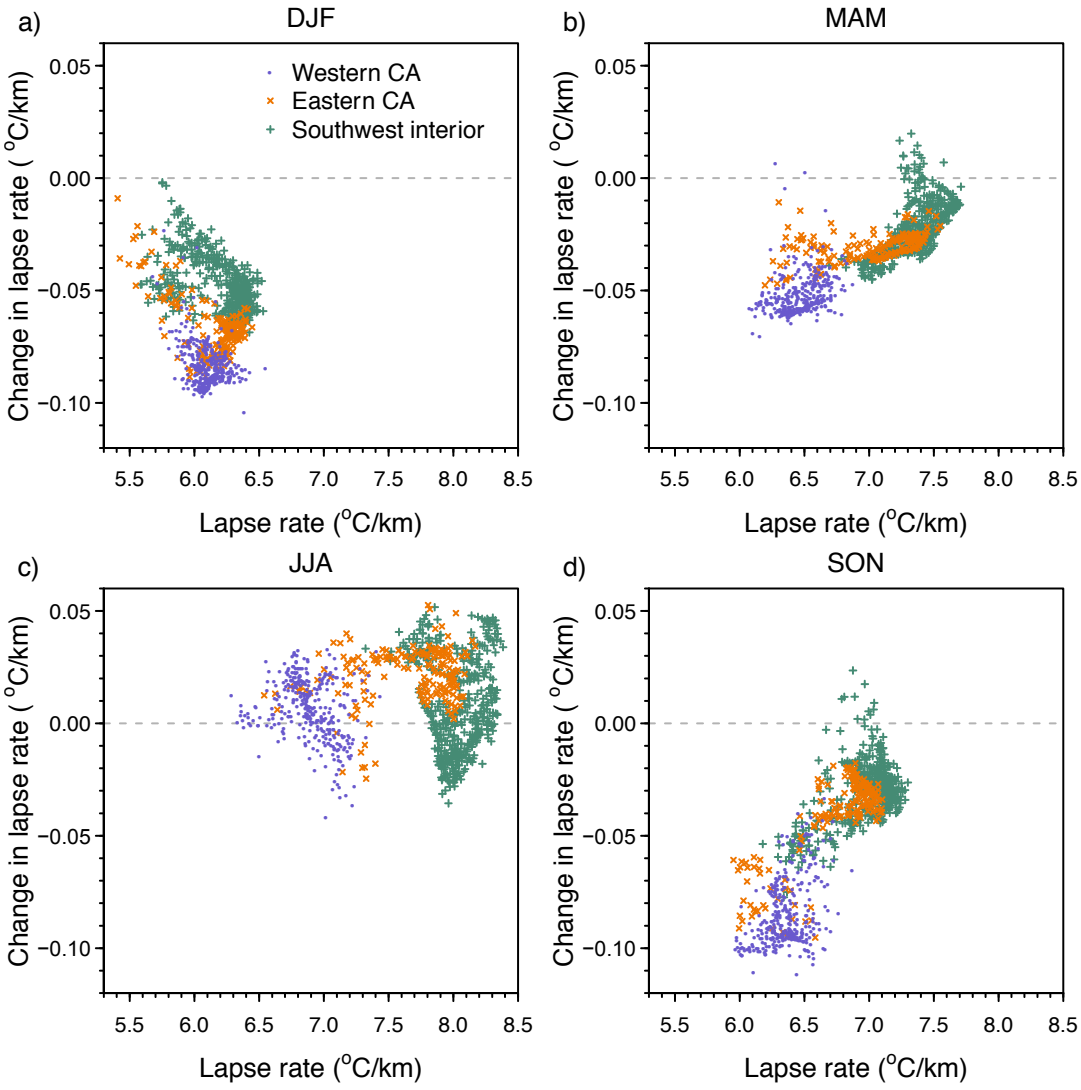

974

975 **Figure 12.** Same as Fig. 11 but for the southwestern US. Note the y-axis ranges differ
976 from Fig. 11.
977

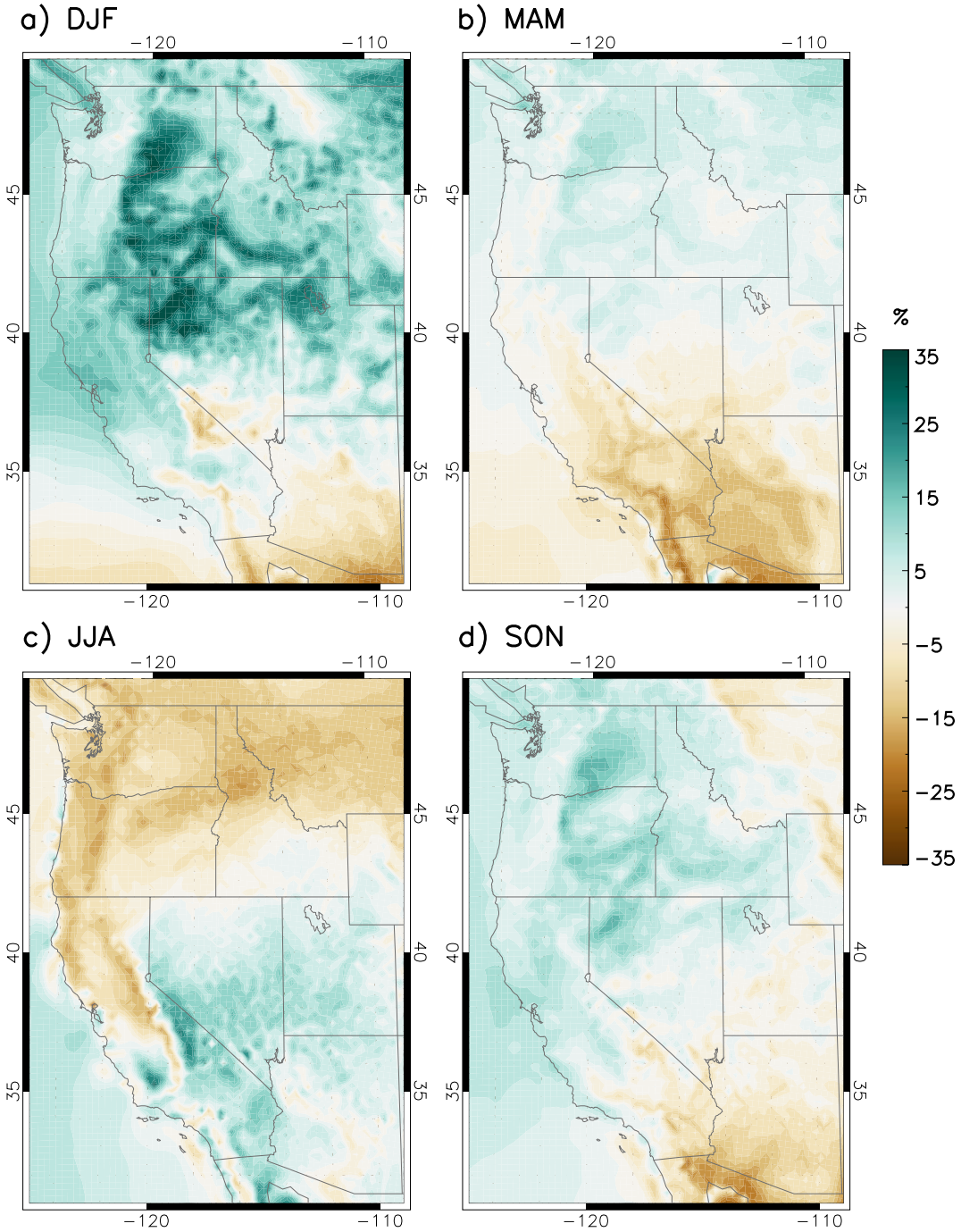

978
979 **Figure 13.** Percent change in ensemble mean seasonal precipitation rate from the
980 historical period to the future scenario.

981

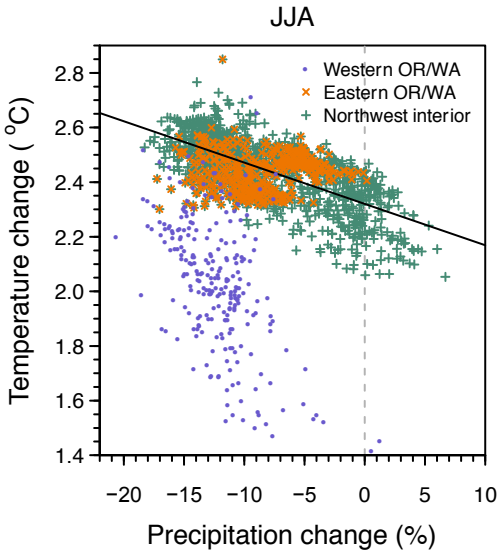

Figure 14. Change in ensemble mean temperature against change in precipitation in summer (JJA) from the historical to the future scenario. The black line shows the linear regression for the Eastern OR/WA and Northwest interior combined. Symbols are colored by sub-domain (see Fig. 1).

Figure1

Click here to download Figure Fig1.tiff

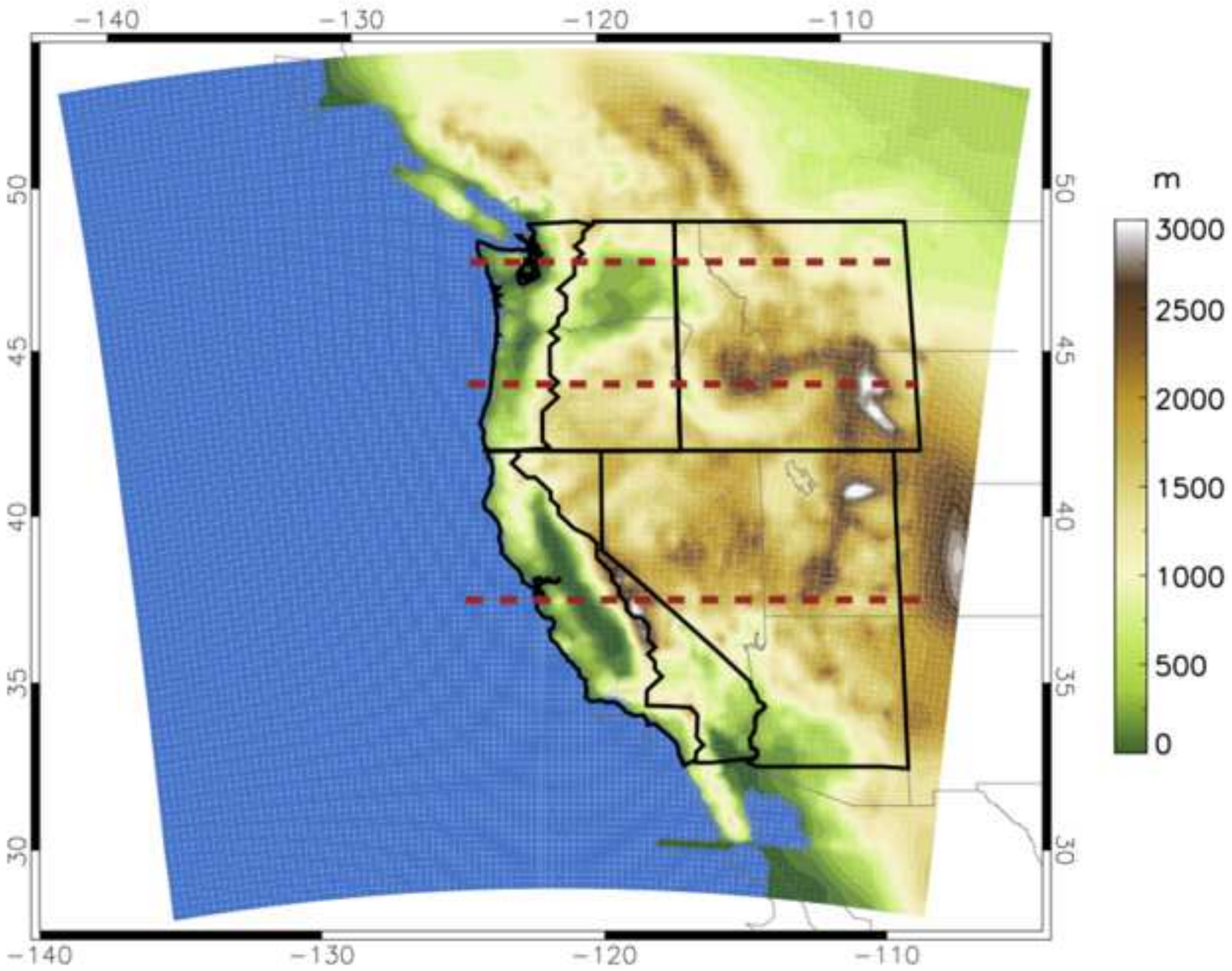

Figure2

Click here to download Figure Fig2.tiff

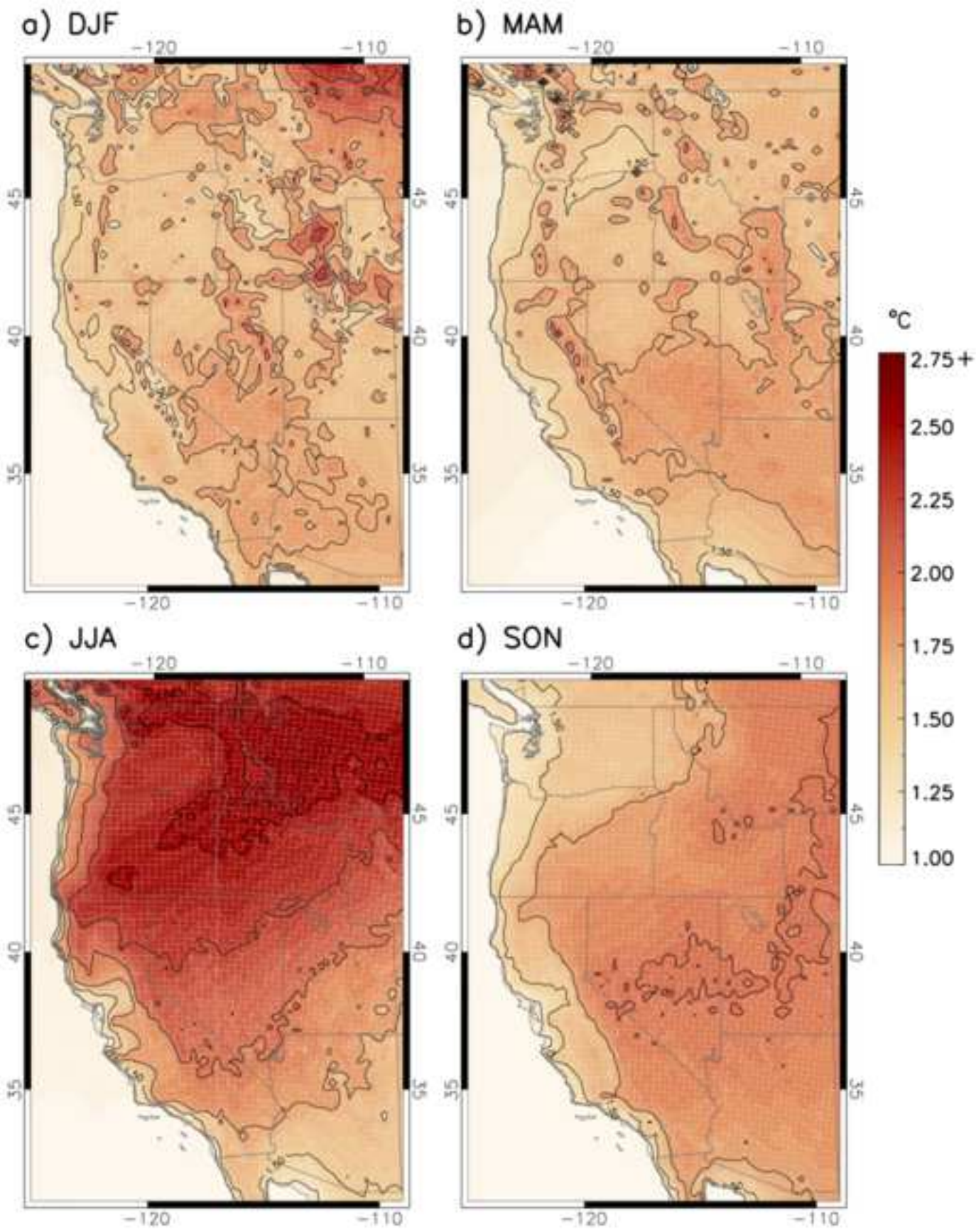

Figure3

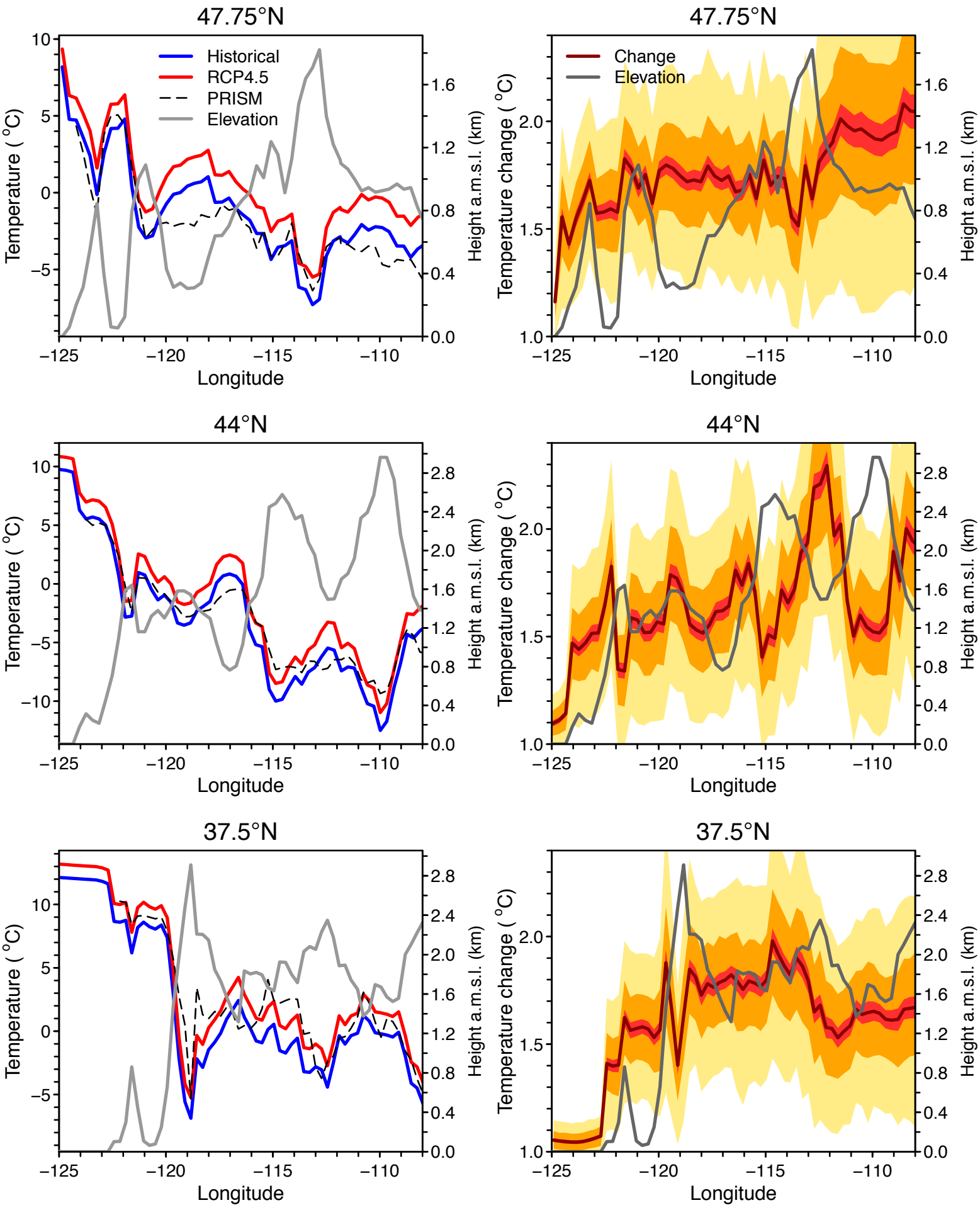
47.75°N
Historical
RCP4.5
PRISM
Elevation
Temperature (°C)
Height a.m.s.l. (km)
Longitude
47.75°N
Change
Elevation
Temperature change (°C)
Height a.m.s.l. (km)
Longitude
44°N
Temperature (°C)
Height a.m.s.l. (km)
Longitude
44°N
Temperature change (°C)
Height a.m.s.l. (km)
Longitude
37.5°N
Temperature (°C)
Height a.m.s.l. (km)
Longitude
37.5°N
Temperature change (°C)
Height a.m.s.l. (km)
Longitude

Figure4

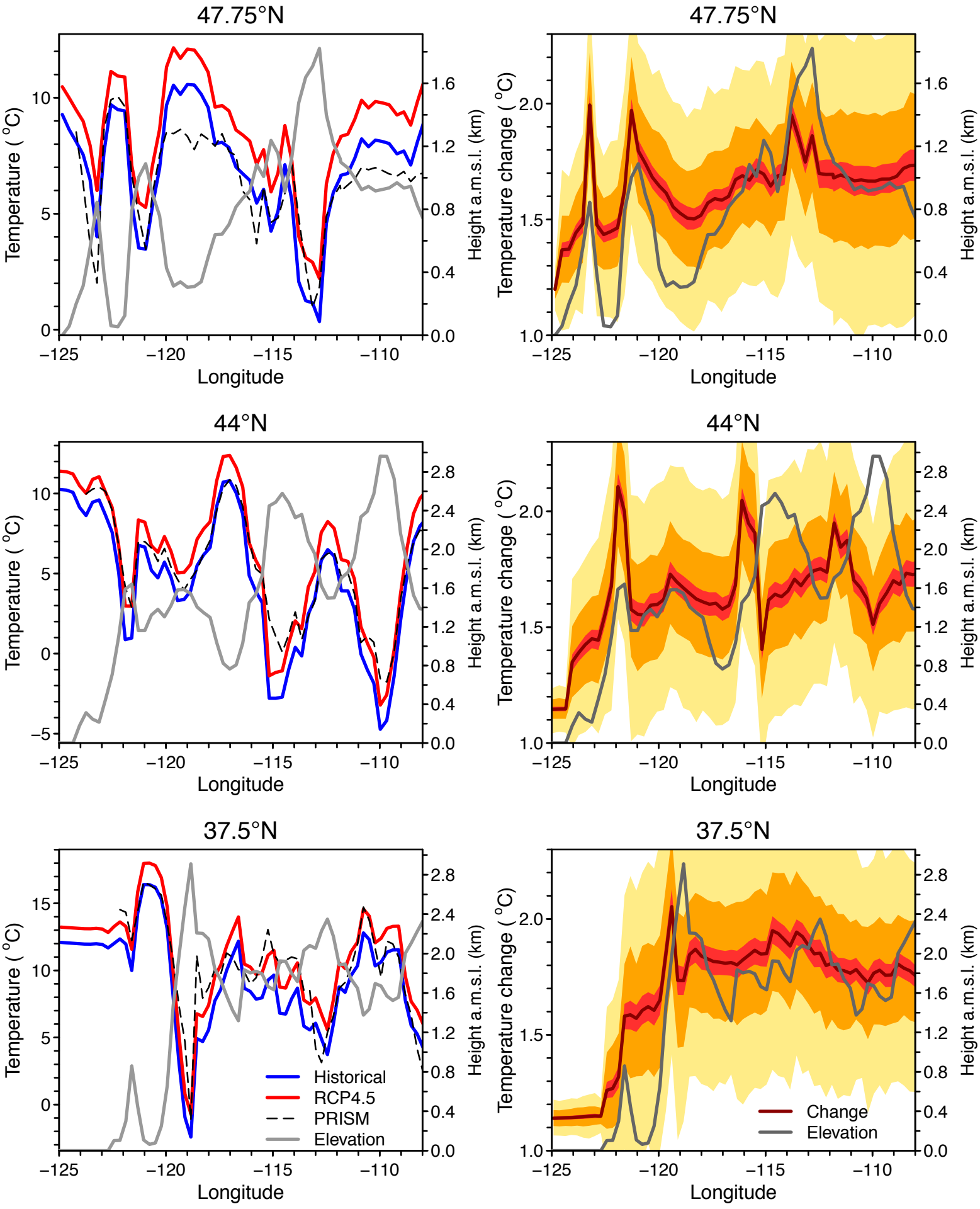
47.75°N
Temperature (°C)
Height a.m.s.l. (km)
Longitude
47.75°N
Temperature change (°C)
Height a.m.s.l. (km)
Longitude
44°N
Temperature (°C)
Height a.m.s.l. (km)
Longitude
44°N
Temperature change (°C)
Height a.m.s.l. (km)
Longitude
37.5°N
Temperature (°C)
Height a.m.s.l. (km)
Longitude
Historical
RCP4.5
PRISM
Elevation
37.5°N
Temperature change (°C)
Height a.m.s.l. (km)
Longitude
Change
Elevation

Figure5

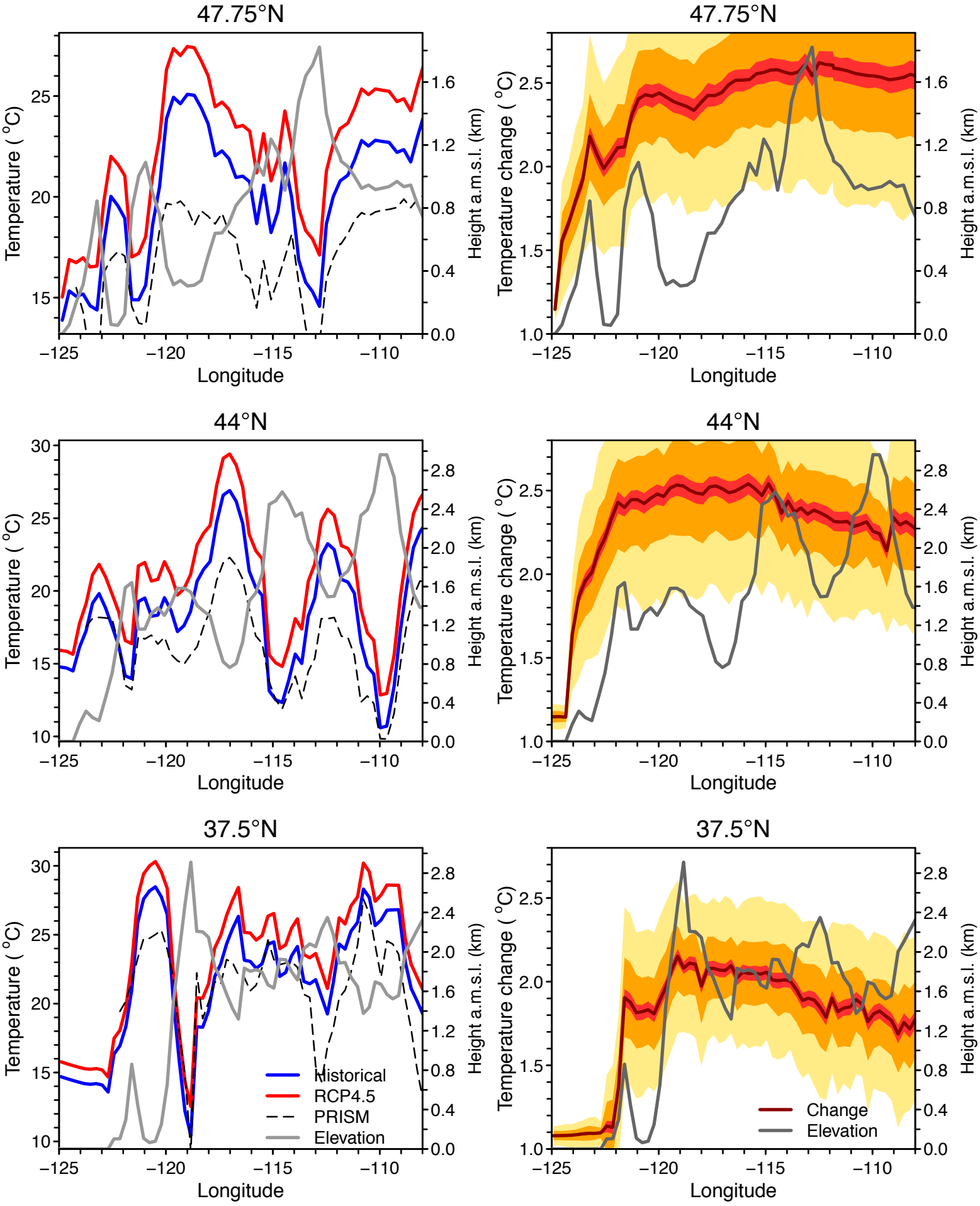
47.75°N
Temperature (°C)
Height a.m.s.l. (km)
Longitude
47.75°N
Temperature change (°C)
Height a.m.s.l. (km)
Longitude
44°N
Temperature (°C)
Height a.m.s.l. (km)
Longitude
44°N
Temperature change (°C)
Height a.m.s.l. (km)
Longitude
37.5°N
Temperature (°C)
Height a.m.s.l. (km)
Longitude
Historical
RCP4.5
PRISM
Elevation
37.5°N
Temperature change (°C)
Height a.m.s.l. (km)
Longitude
Change
Elevation

Figure6

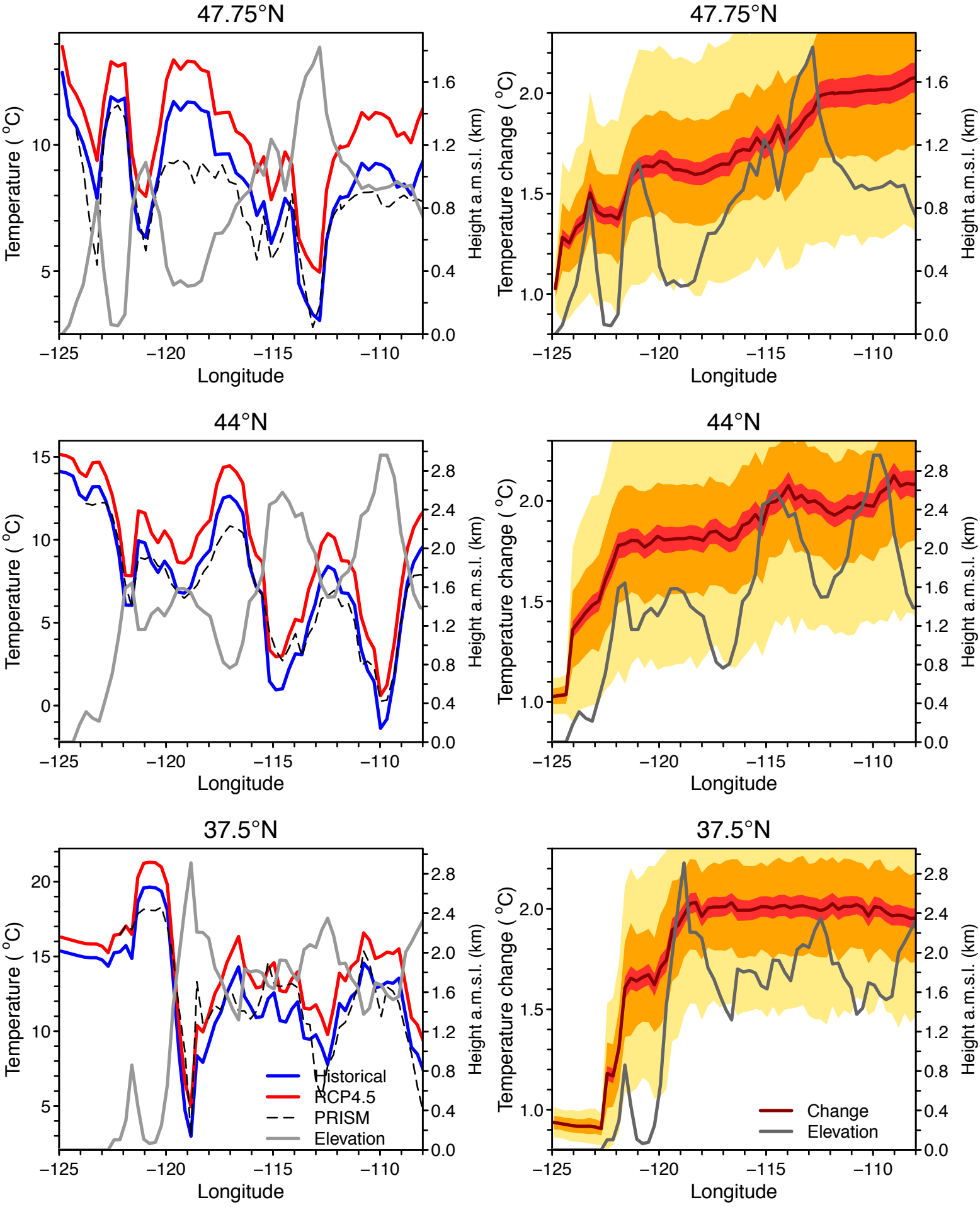
47.75°N
Temperature (°C)
Height a.m.s.l. (km)
Longitude
47.75°N
Temperature change (°C)
Height a.m.s.l. (km)
Longitude
44°N
Temperature (°C)
Height a.m.s.l. (km)
Longitude
44°N
Temperature change (°C)
Height a.m.s.l. (km)
Longitude
37.5°N
Temperature (°C)
Height a.m.s.l. (km)
Longitude
Historical
RCP4.5
PRISM
Elevation
37.5°N
Temperature change (°C)
Height a.m.s.l. (km)
Longitude
Change
Elevation

Figure7

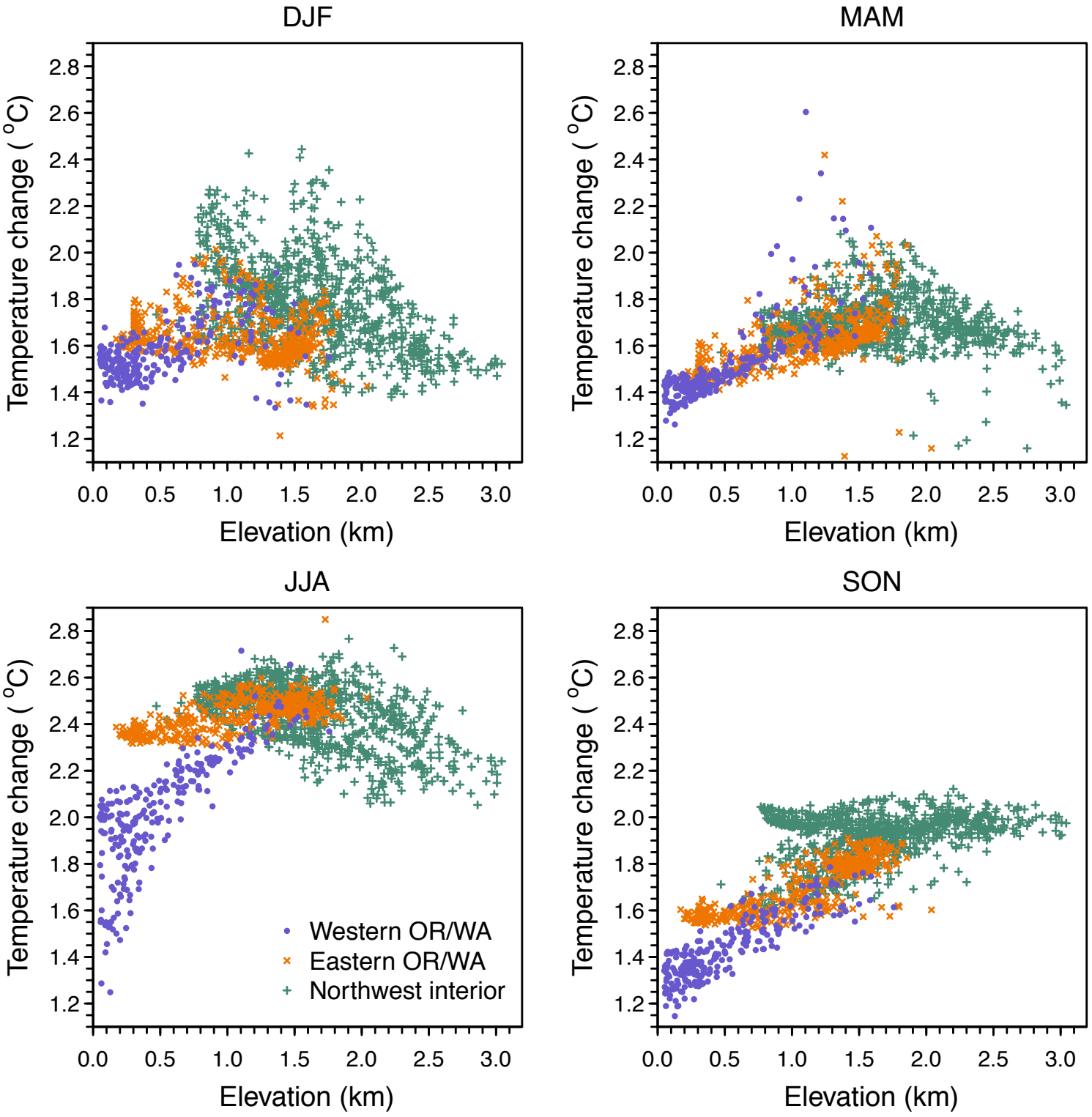
DJF
MAM
JJA
SON
Temperature change (°C)
Elevation (km)
1.2
1.4
1.6
1.8
2.0
2.2
2.4
2.6
2.8
0.0
0.5
1.0
1.5
2.0
2.5
3.0
Western OR/WA
Eastern OR/WA
Northwest interior

Figure8

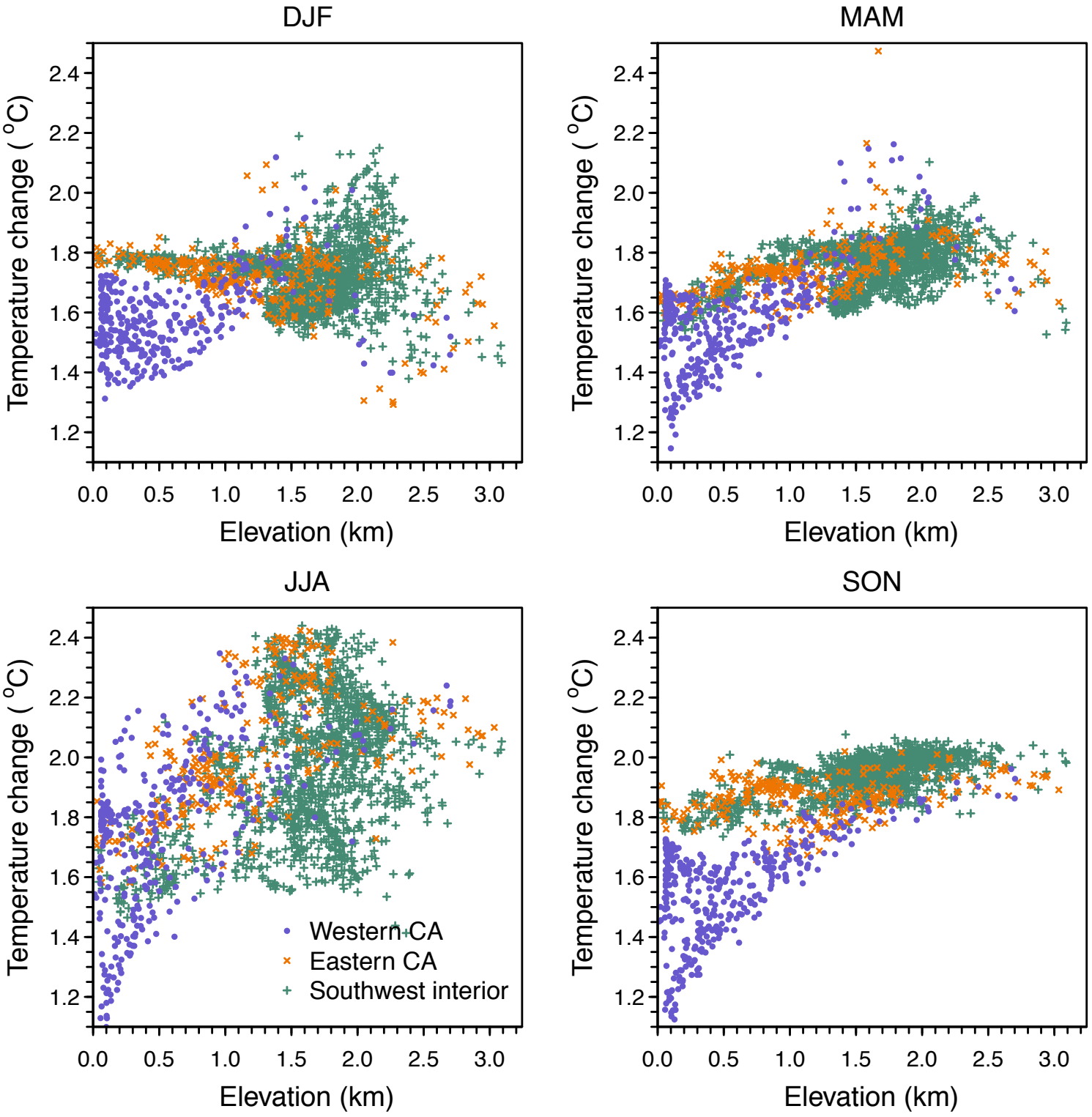
DJF
MAM
JJA
SON
Temperature change (°C)
Elevation (km)
1.2
1.4
1.6
1.8
2.0
2.2
2.4
0.0
0.5
1.0
1.5
2.0
2.5
3.0
Western CA
Eastern CA
Southwest interior

Figure9

Click here to download Figure Fig9.tiff

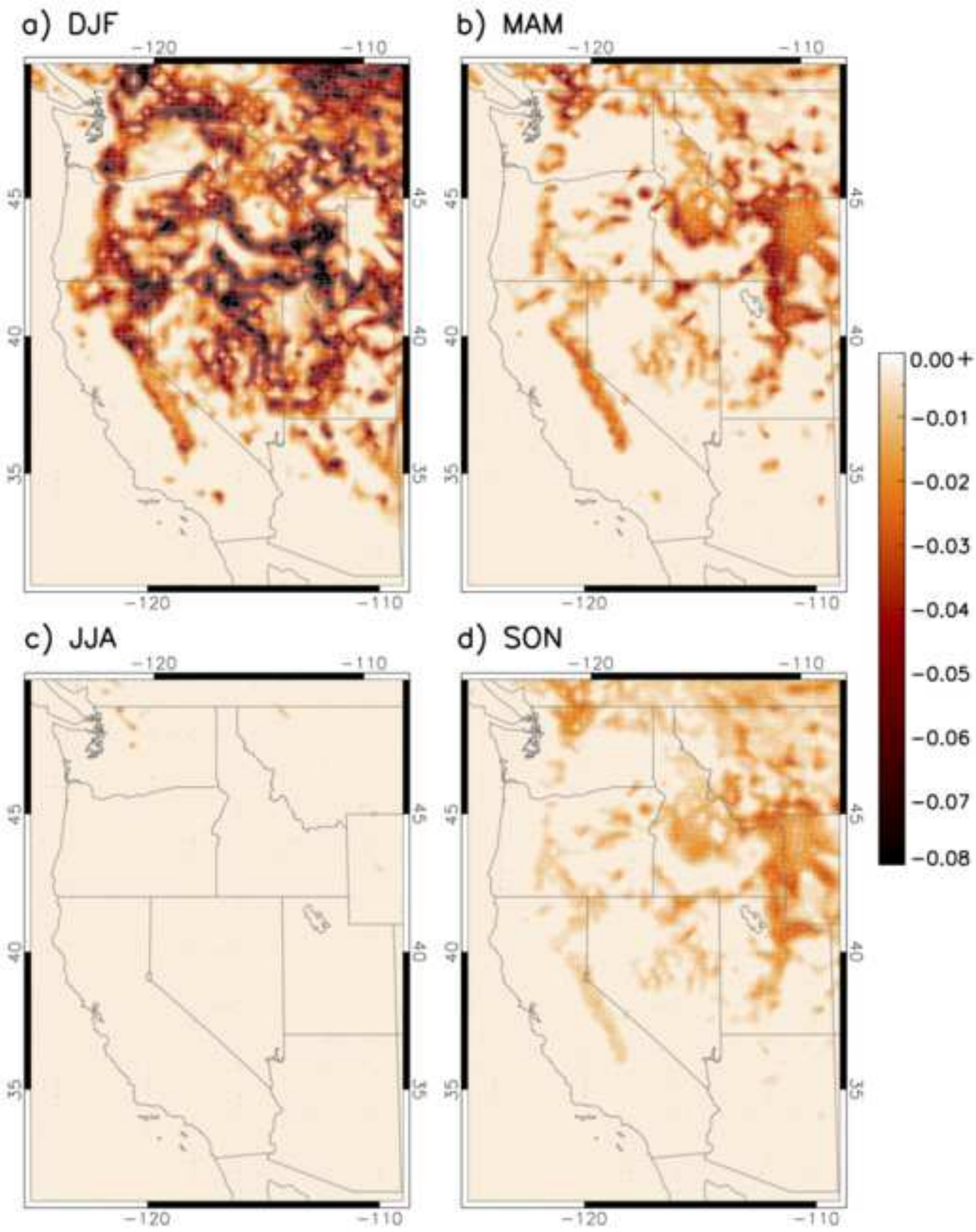

Figure10

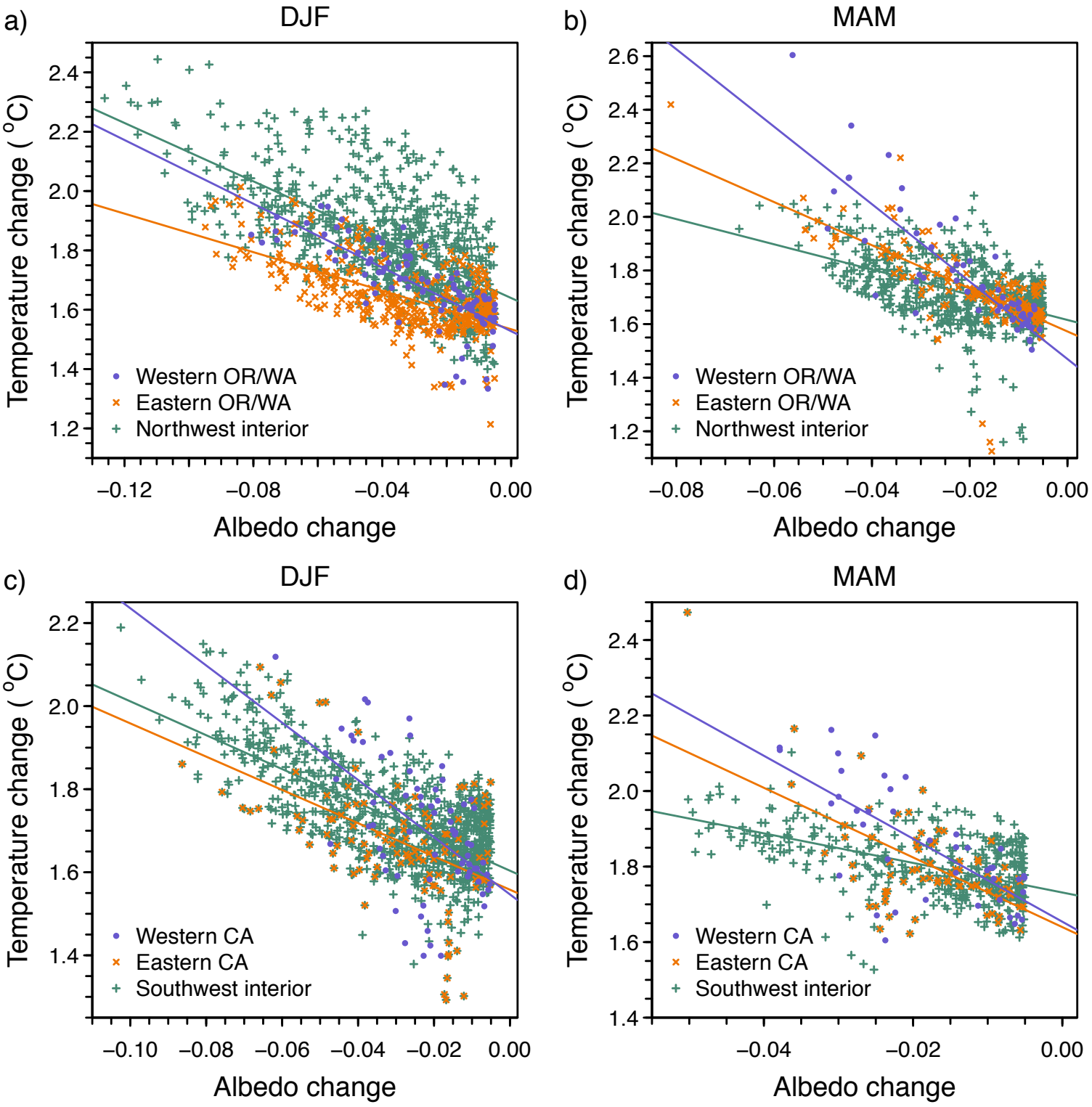
a)
DJF
Temperature change (°C)
Albedo change
Western OR/WA
Eastern OR/WA
Northwest interior
b)
MAM
Temperature change (°C)
Albedo change
Western OR/WA
Eastern OR/WA
Northwest interior
c)
DJF
Temperature change (°C)
Albedo change
Western CA
Eastern CA
Southwest interior
d)
MAM
Temperature change (°C)
Albedo change
Western CA
Eastern CA
Southwest interior

Figure11

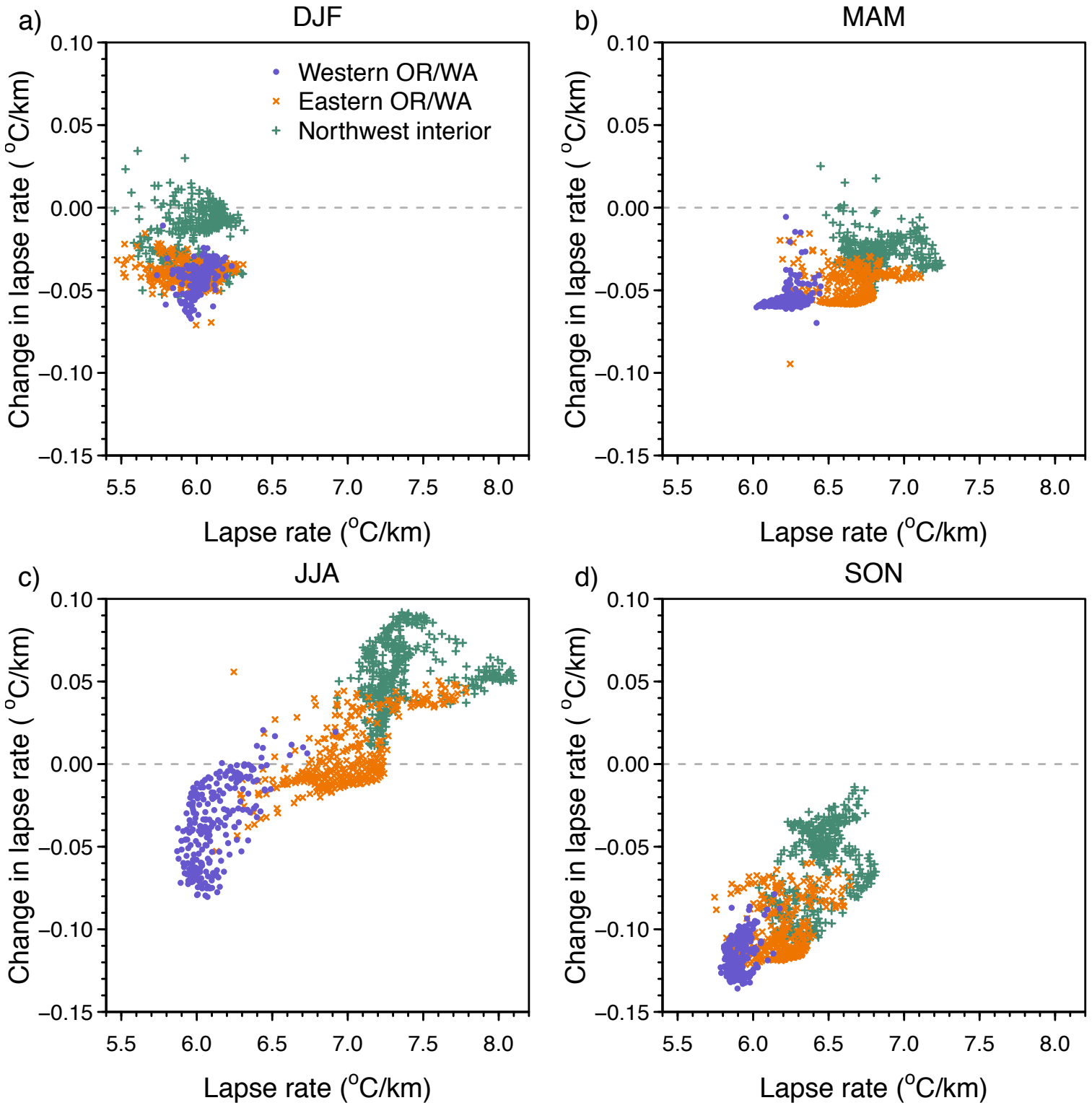
a)
DJF
b)
MAM
c)
JJA
d)
SON
Western OR/WA
Eastern OR/WA
Northwest interior
Change in lapse rate (°C/km)
Lapse rate (°C/km)
0.10
0.05
0.00
−0.05
−0.10
−0.15
5.5
6.0
6.5
7.0
7.5
8.0

Figure12

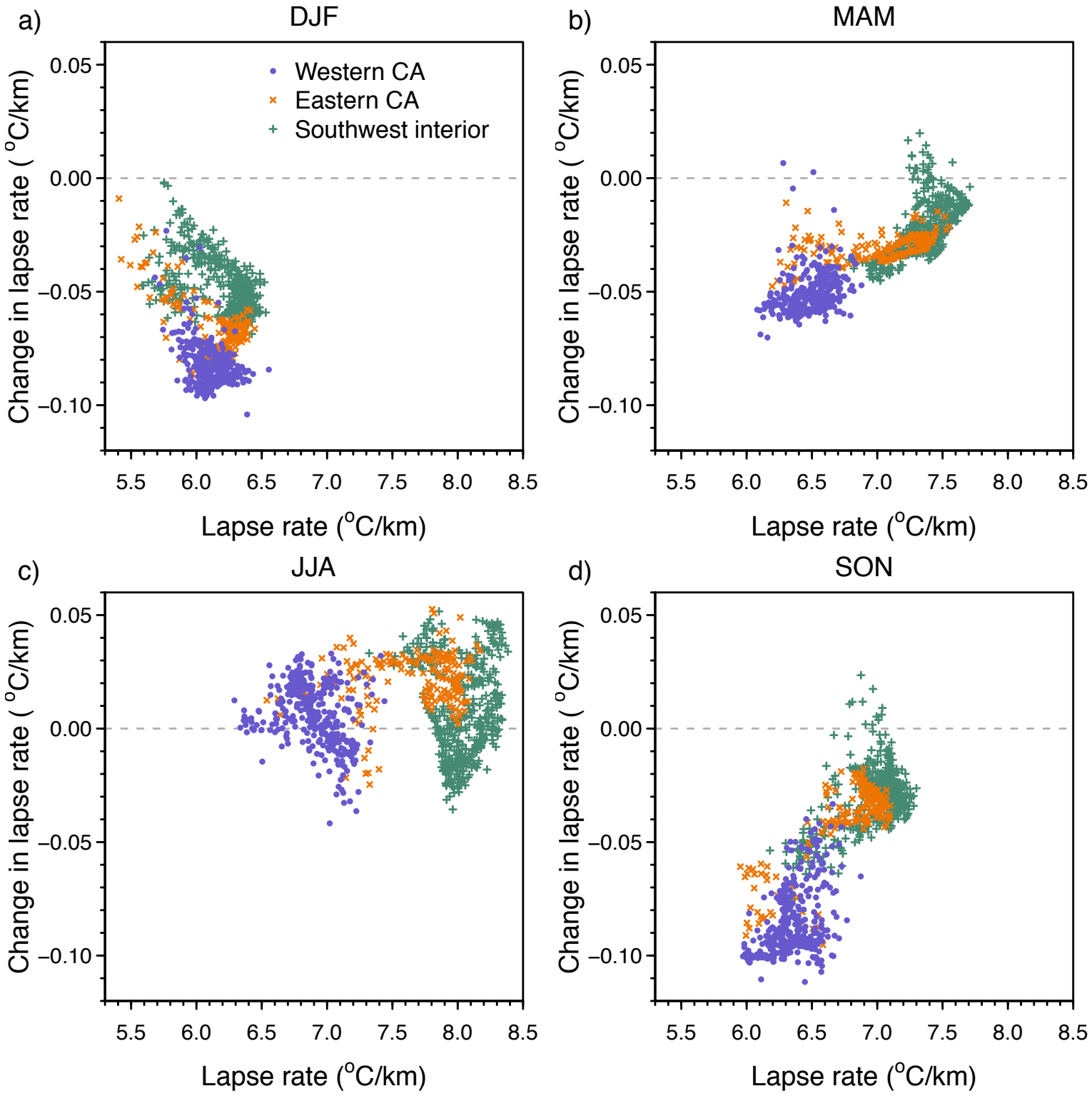
a)
DJF
b)
MAM
c)
JJA
d)
SON
Western CA
Eastern CA
Southwest interior
Change in lapse rate (°C/km)
Lapse rate (°C/km)
0.05
0.00
−0.05
−0.10
5.5
6.0
6.5
7.0
7.5
8.0
8.5

Figure13

Click here to download Figure Fig13.tiff

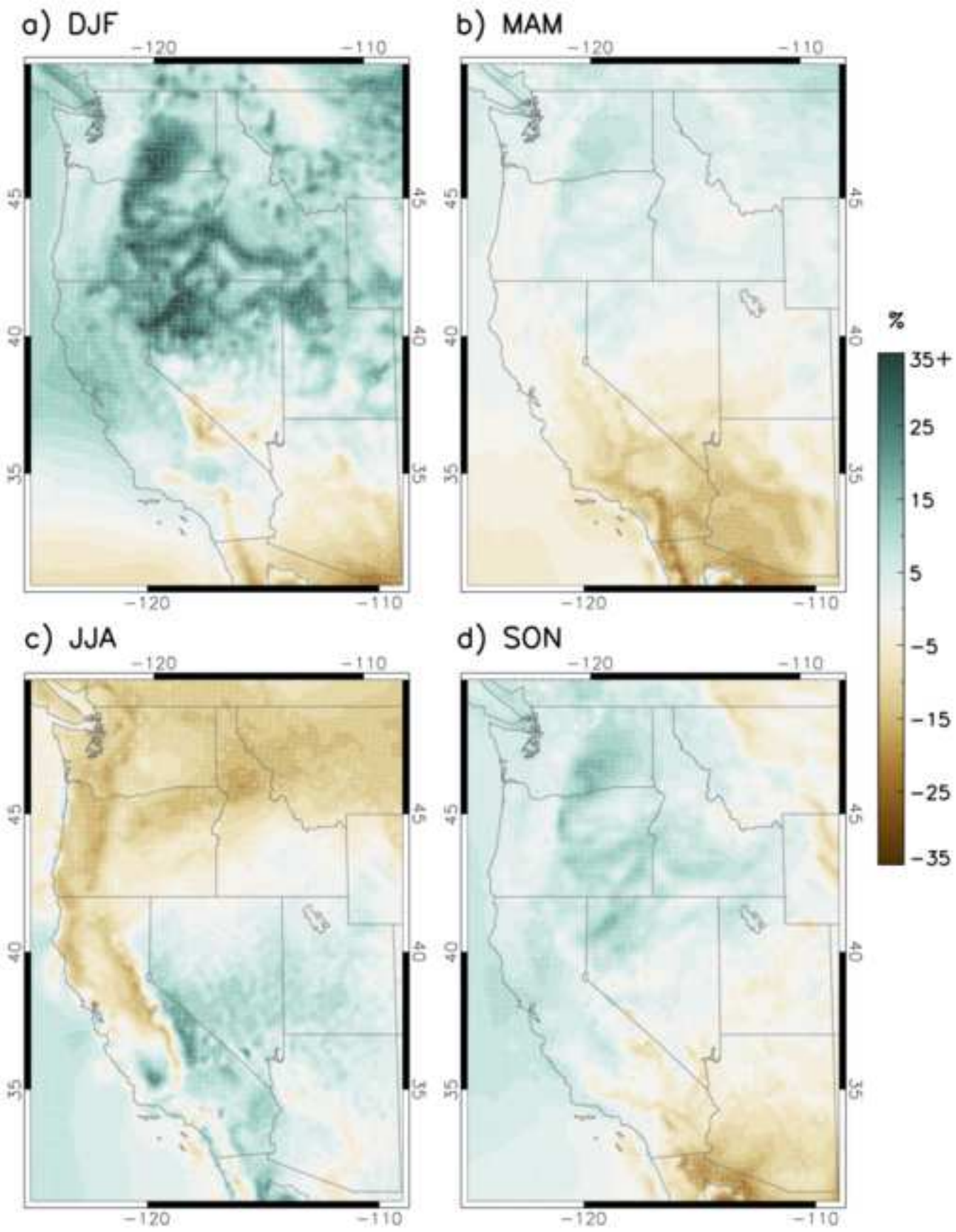

Figure14

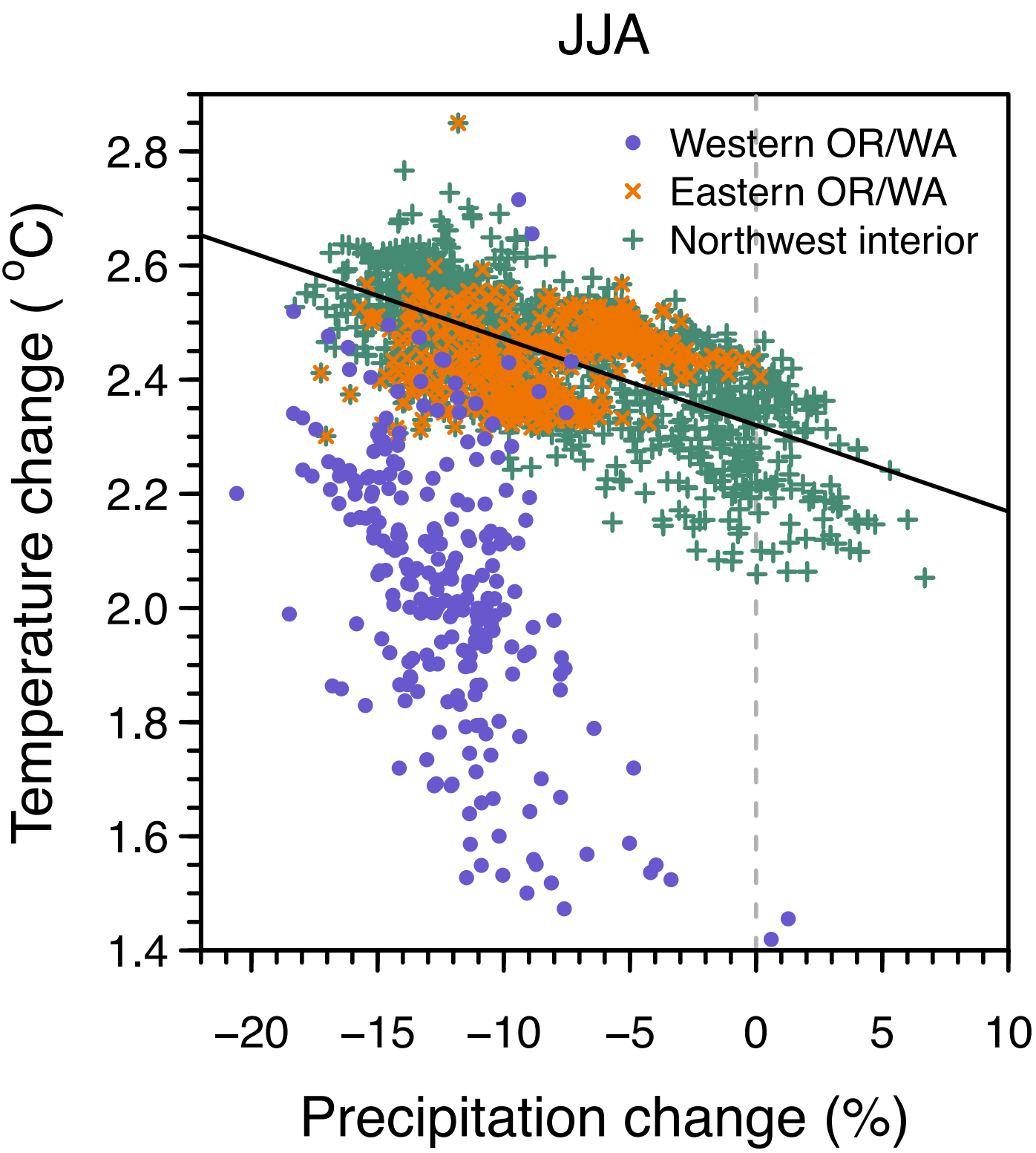
JJA
Western OR/WA
Eastern OR/WA
Northwest interior
Temperature change (°C)
2.8
2.6
2.4
2.2
2.0
1.8
1.6
1.4
–20
–15
–10
–5
0
5
10
Precipitation change (%)

Table 1. Slope of the linear relationship between the change in temperature (T) and the decrease in albedo (α) given as the change in T for a -0.1 change in α from the historical period to the future scenario for $\Delta\alpha < -0.0002$.

Region	Winter (DJF)			Spring (MAM)		
	$-0.1\Delta T/\Delta\alpha$ (°C)	Inner 95% C.I.	R^2	$-0.1\Delta T/\Delta\alpha$ (°C)	Inner 95% C.I.	R^2
Western WA/OR	0.55	0.49, 0.60	0.51	1.39	1.24, 1.55	0.76
Eastern WA/OR	0.26	0.23, 0.30	0.32	0.80	0.72, 0.88	0.55
Northwest Interior	0.54	0.51, 0.57	0.68	0.38	0.33, 0.42	0.24
Western CA	0.69	0.55, 0.83	0.41	1.25	1.08, 1.41	0.70
Southwest Interior[1]	0.30	0.28, 0.32	0.32	0.34	0.30, 0.39	0.19

[1]Merged with eastern CA